

**UNIVERSITATEA POLITEHNICA DIN BUCUREȘTI  
ȘCOALA DOCTORALĂ CHIMIE APLICATĂ ȘI ȘTIINȚA  
MATERIALELOR**



**Sisteme cu eliberare țintită de substanțe farmaceutic  
active**

---

**Targeted delivery systems for active pharmaceutical  
ingredients**

**SUPERVISOR**

**Prof.dr.eng. Daniela Berger**

**AUTHOR**

**Eng. Doina Georgescu**

**BUCHAREST 2017**

*Keywords:* drug delivery systems; targeted delivery systems; magnetite; cobalt ferrite; magnetic composites; magnetite-silica; cobalt ferrite-mesoporous silica composite; SBA-15-type silica-titania composites

## Content

Part I. Literature data	7
I.1 Introduction	7
I.2 Synthesis and properties of mesoporous silica with hexagonal pore array	9
I.3 Applications of mesoporous silica in biomedicine	12
I.3.1 Influence of mesoporous material textural parameters on the adsorption of biologically active molecules	15
I.3.2 Multifunctional mesoporous silica-based materials	17
I.3.3 Examples of mesoporous silica carriers	19
I.4 Importance of magnetic particles for biomedicine	30
I.4.1 Magnetic properties of materials	30
I.4.2 Applications of magnetic nanoparticles and magnetic composite materials	35
I.4.3 Synthesis methods of magnetic nanoparticles	42
I.4.4 Encapsulation of magnetic nanoparticles	47
I.5 Silica-titania mesoporous composite materials	49
I.5.1 Synthesis and characterization of silica-titania mesoporous composite materials	49
I.5.2 Effect of titanium incorporation on the hydrophilic nature of TiSBA-15 composite material surface	56
I.5.3 Applications of silica-titania composite materials	57
References	60
Part II. Original contributions	76
II.1 Justification of theme	76
II.2 Investigation methods of synthesized compounds	77
II.3 Synthesis and characterization of magnetic nanoparticles	80
II.3.1 Obtaining and characterization of mesoporous ferrites in the presence of copolymer P123	80
II.3.2 Obtaining and characterization of ferrite nanoparticles in the presence of oleic acid	87
II.3.3 Synthesis of magnetite in the presence of CTAB	91
II.4 Encapsulation of ferrite nanoparticles in mesoporous silica	94
II.4.1 Synthesis and characterization of magnetic composite materials	96
II.4.1.1 Studies on cellular toxicity of magnetic composite materials	103
II.4.2 Synthesis and characterization of Fe <sub>3</sub> O <sub>4</sub> @MCM-41 magnetic composites in the presence of CTAB	104
II.4.3 Conclusions on the synthesis and properties of the magnetic materials	109
II.5 Antibiotics delivery systems	112
II.5.1 Synthesis and characterization silica-titania mesoporous composite materials	112
II.5.2 Evaluation of silica-titania mesoporous composite materials in drug delivery systems	118
II.5.2.1 Synthesis and characterization of oxytetracycline-loaded silica-titania composites	120
II.5.2.2 <i>In vitro</i> release profiles of oxytetracycline from silica-titania mesoporous composites	123
II.5.2.3 Antimicrobial activity of oxytetracycline delivery systems	127
II.5.3 Mesoporous titania as carrier in drug delivery systems	128
II.5.3.1 Synthesis and characterization of mesoporous titania	128
II.5.3.2 Testing of mesoporous titania as a carrier for oxytetracycline	136
II.5.3.3 <i>In vitro</i> release profile of oxytetracycline	138
II.5.4 Conclusions on the application of silica-titania mesoporous composites as carriers of biologically active molecules	139
II.6 Doxorubicin targeted delivery systems	141
II.6.1 Synthesis of magnetic nanoparticles obtained from Fe(acac) <sub>3</sub>	144
II.6.2 Synthesis and characterization magnetic carriers	147
II.6.3 Synthesis and characterization doxorubicin targeted delivery systems	157
II.6.4 <i>In vitro</i> doxorubicin release studies from magnetite-mesoporous silica-type carriers	161
II.6.5 Toxicity assays on doxorubicin targeted delivery systems	165
II.6.6 Partial conclusions about doxorubicin targeted delivery systems	167

## Part II. Original contributions

### II.1 Justification of theme

This PhD thesis, *Targeted delivery systems for active pharmaceutical ingredients*, falls within an interdisciplinary field of nanotechnology applied in biomedicine. Because cancer is the main cause of mortality, the development of modern therapies by developing antitumor targeted delivery systems, which can lead to increase the life expectancy by improving treatment efficiency is very important. Currently, many interdisciplinary research groups work in the field of drug delivery systems.

The purpose of this PhD thesis was *the development of antitumor targeted delivery systems based on inorganic carriers containing pure and functionalized mesoporous silica*. As cytostatic agent, doxorubicin, which has a high toxicity being used in the chemotherapy of leukemia, Hodgkin's lymphoma and stomach, breast, lungs, ovaries cancer, etc was chosen as model drug for the development of targeted drug delivery systems.

In order to achieve the aim of this PhD thesis, the following objectives were established:

- ✓ Synthesis and characterization of superparamagnetic ferrite nanoparticles
- ✓ Encapsulation of ferrite nanoparticles in pristine and functionalized mesoporous silica to obtain magnetic carriers that can accommodate enough amount of therapeutic agent
- ✓ Characterization of magnetic carriers by various techniques: X-ray diffraction, FTIR spectroscopy, scanning and transmission electron microscopy, N<sub>2</sub> adsorption-desorption isotherms, magnetic measurements at room temperature.
- ✓ Encapsulation of doxorubicin in magnetic inorganic carriers.
- ✓ Characterization of targeted doxorubicin delivery systems based on magnetic carriers.
- ✓ Determination of *in vitro* doxorubicin release profiles from magnetic carriers.

Another objective of this thesis was the obtaining and characterization of mesostructured SBA-15-type silica-titania composites, which can be used as carriers for various active pharmaceutical ingredients. These mesoporous composites were compared to SBA-15 silica and mesoporous titania. In this study, as a model molecule was chosen oxytetracycline, a broad spectrum antibiotic from the tetracyclines class.

### II.3 Synthesis and characterization of magnetic nanoparticles

#### II.3.1 Obtaining and characterization of mesoporous ferrite in the presence of copolymer P123

In the PhD thesis, the ferrite nanoparticles were obtained by co-precipitation method in the presence of different stabilizers and through the decomposition of complex compounds were.

Among stabilizers, Pluronic P123 triblock copolymer, which also acts as a pore-forming agent, was used. For the preparation of magnetite nanoparticles, 0.1875 g of Pluronic P123 was dissolved under magnetic stirring in 30 mL 1:1 (vol) water : ethanol. Iron salts were dissolved, (4.9819 g iron (III) chloride and 2.5668 g iron (II) sulfate) in a minimum volume of water, after which the solution of iron salts was added to the Pluronic P123 solution.

The resulting mixture was maintained at 40 °C under argon atmosphere to avoid oxidation of divalent iron ions under mechanical agitation. After 1 hour, 20 mL of precipitating agent, 25% (wt) aqueous ammonia solution were poured into the reaction mixture containing iron ions. The

reaction mixture was mechanically stirred for 1 h and the resulting black solid was recovered and washed with a mixture of 1:1 (vol) water : ethanol by magnetic decantation [6].

Cobalt ferrite nanoparticles were obtained similarly by using as precursors 2.1968 g cobalt chloride, 4.9819 g iron (III) chloride and 10 mL 10 M aqueous solution NaOH as precipitating agent. Synthesis of the cobalt ferrite was performed in the presence of the same stabiliser, Pluronic P123 triblock copolymer (0.1875 g Pluronic P123 dissolved in 30 mL of 1:1 (vol) water : ethanol mixture), as in the case of magnetite. In the case of cobalt ferrite a long ageing step at 60°C for 20 h was necessary to obtain crystalline oxide powder [6].

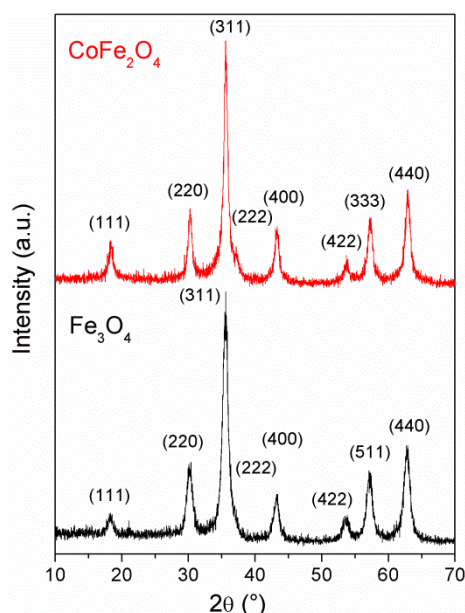


Fig.II.2.XRD patterns of magnetite and cobalt ferrite nanopowders obtained in the presence of Pluronic P123

Both magnetite and cobalt ferrite powders presented inverse spinel structure with cubic symmetry demonstrated by powder X-ray diffraction analysis (Fig.II.2). Magnetite and cobalt ferrite were indexed according ICDD 79-0418 and ICDD 22-1086, respectively. The unit cell parameter of magnetite was 7.0137 Å, while for  $\text{CoFe}_2\text{O}_4$ , a lower value was obtained, 6.9813 Å. The crystallite size was computed using Rigaku PDXL software based on Sherrer's equation from all diffraction peaks. The crystallite size was smaller for magnetite (9 nm) than for  $\text{CoFe}_2\text{O}_4$  (12 nm) [6].

The oxide nanopowders were also investigated by FTIR spectroscopy in order to assess the formation of inverse spinel structure characteristic for ferrites and the interactions between oxide nanoparticles and the polymer used as capping agent. It has been demonstrated that the interactions between Pluronic copolymer and the surface of inverse spinel structure ferrite are not strong as the stabiliser has been removed during the isolation and washing of samples, the main role of the polymer being the formation of interparticle mesopores.

The characteristic stretching vibrations of Fe-O bonds in FTIR spectrum of  $\text{Fe}_3\text{O}_4$  can be noticed at 450, 580 and 630  $\text{cm}^{-1}$  and correspond to Fe(II)-O and Fe(III)-O bonds in both octahedral and tetrahedral geometries [7-9]. The polymer bands used as porogen agent are hardly visible in the FTIR spectrum for  $\text{Fe}_3\text{O}_4$  [6].

The morphology of magnetite and cobalt ferrite samples was investigated by scanning electron microscopy. The samples presented similar morphology having nanosized spherical particles, with narrow size distribution having the tendency to form spherical agglomerates (Fig. II.4). TEM investigation of  $\text{CoFe}_2\text{O}_4$  nanopowder showed the presence of small particles with the diameter in the range of 8-16 nm. One can notice that the porosity of the sample resulted due to interparticle pores (Fig. II.5) [6].

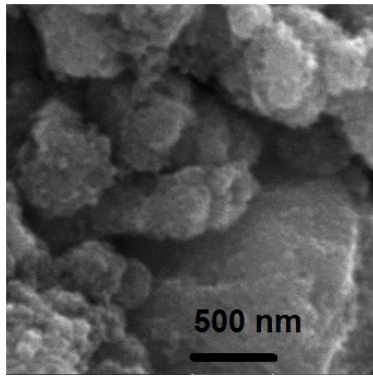


Fig.II.4 SEM micrographs of Fe<sub>3</sub>O<sub>4</sub> (left) and CoFe<sub>2</sub>O<sub>4</sub> (right)

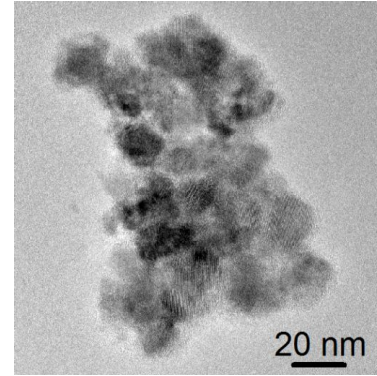
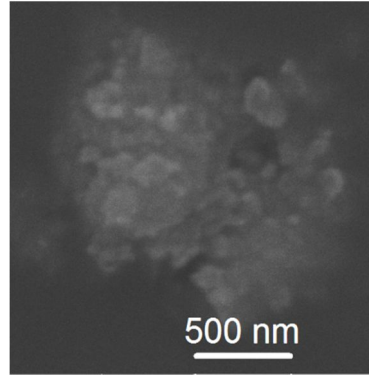


Fig.II.5 TEM micrograph of CoFe<sub>2</sub>O<sub>4</sub>

The N<sub>2</sub> adsorption-desorption isotherms for both ferrites synthesized in the presence of Pluronic P123 are type IV with H1 hysteresis loop typical for mesoporous materials (Fig.II.6). The textural parameters of ferrite samples (specific surface area,  $S_{BET}$ , total pore volume,  $V_p$  and average pore diameter,  $d_{BJH}$ ) are listed in Table II.1. The total pore volumes were determined at relative pressure,  $P/P_0=0.9900$ , specific surface area values were computed using Brunauer–Emmett–Teller (BET) method from multi-point regression in the 0.05-0.30 relative pressure range, while the pore size distribution curves were computed by Barrett-Joyner-Halenda model based on Kelvin equation from the isotherm desorption branch. Both samples exhibited unimodal pore size distribution, lower value of average pore diameter (8.34 nm) being determined for CoFe<sub>2</sub>O<sub>4</sub> than for magnetite (11.42 nm). Both samples have the pores dimension in the range of mesopores. Also, Fe<sub>3</sub>O<sub>4</sub> and CoFe<sub>2</sub>O<sub>4</sub> have high values of specific surface area (120 and 155 m<sup>2</sup>/g, respectively).

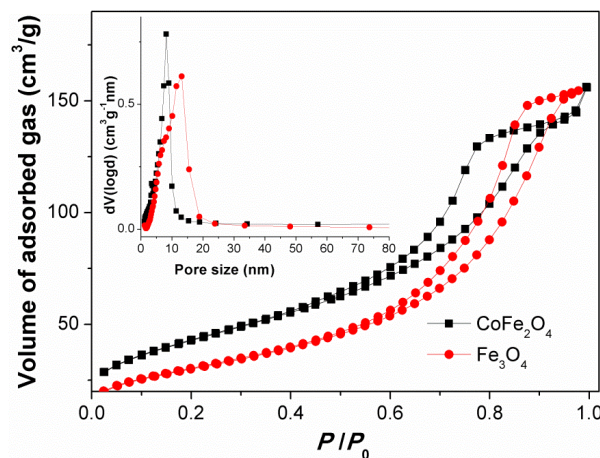


Fig.II.6 N<sub>2</sub> adsorption-desorption isotherms of Fe<sub>3</sub>O<sub>4</sub> and CoFe<sub>2</sub>O<sub>4</sub> nanopowders

Table II.1 Properties of synthesized spinel ferrites

Probă	$M_s$ (emu/g)	$\chi_g \times 10^6$	$M_r/M_s$	$S_{BET}$ (m <sup>2</sup> /g)	$V_p$ (cm <sup>3</sup> /g)	$d_{BJH}$ (nm)
Fe <sub>3</sub> O <sub>4</sub>	49.73	970.26	0	120	0.24	11.42
CoFe <sub>2</sub> O <sub>4</sub>	42.47	583.30	0.257	155	0.24	8.34

The magnetic properties of magnetite and cobalt ferrite were studied by measuring the magnetization as function of applied magnetic field in the range of -10000 – +10000 Oe. At a given applied magnetic field, the magnetization depends on the magnetic moment, which is influenced by the particle size. The total magnetization is a sum of three components: ferromagnetic (hysteretic magnetization), superparamagnetic (fitted by a Langevin function) and paramagnetic [1,2]. It can be noticed that either magnetite or cobalt ferrite did not reach the

saturation magnetization, these values being determined by fitting the experimental data considering the ferromagnetic and paramagnetic contributions for cobalt ferrite that exhibited a ferrimagnetic behavior and the superparamagnetic component for  $\text{Fe}_3\text{O}_4$ . The magnetization loop of magnetite shows zero coercivity and zero remanence proving its superparamagnetic behavior (Fig II.8). The saturation magnetization of  $\text{Fe}_3\text{O}_4$  (49.73 emu/g) is lower than for magnetite obtained similarly by coprecipitation in the presence of trimethylhexadecylammonium bromide (59.81 emu/g) [10]. Cobalt ferrite capped in P123 has high coercivity,  $H_c=468.87$  Oe, and a remnant magnetization of 10.93 emu/g, demonstrating a ferrimagnetic behavior (Table II.1), its saturation magnetization being 42.47 emu/g, lower value than for cobalt ferrite capped in oleic acid (52.33 emu/g), having the average particle size of 13 nm [11].

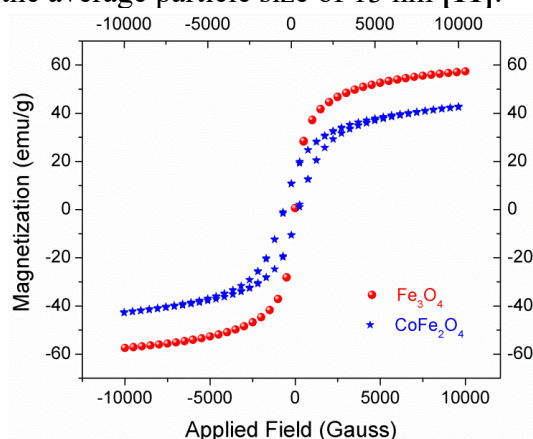


Fig.II.8 Magnetization versus applied filed for mesoporous ferrite nanopowders

### II.3.2 Obtaining and characterization of ferrite nanoparticles in the presence of oleic acid

Magnetite and cobalt ferrite were similarly synthesized, also by coprecipitation, but oleic acid was used as stabilizer. In comparison with the synthesis of magnetic nanoparticles in the presence of Pluronic P123 at 40 °C, the preparation of magnetite and cobalt ferrite nanoparticles using oleic acid was carried aout at room temperature and 90 °C, respectively. For the synthesis of magnetite, the metal precursors were  $\text{FeCl}_3 \cdot 6\text{H}_2\text{O}$  and  $\text{FeCl}_2 \cdot 4\text{H}_2\text{O}$ , while for cobalt ferrite,  $\text{FeCl}_3 \cdot 6\text{H}_2\text{O}$  and  $\text{CoCl}_2 \cdot 6\text{H}_2\text{O}$  were used. Moreover, the same precipitation agents were used, in the case of magnetite, e 25%(wt.) concentrated ammonia solution [14], and for cobalt ferrite, 10 M NaOH aqueous solution. In order to obtain crystalline cobalt ferrite, a long aging step of formed precipitate was necessary, the time and temperature at which the process was carried out being similar to the cobalt ferrite obtained in the presence Pluronic P123.

Briefly, 30 ml of deionized water was purjed with argon for 10 min and then the solid salts (for the preparation of the magnetite, iron trichloride and iron dichloride and for cobalt ferrite, iron trichloride, and cobalt dichloride), as well as oleic acid were added in the reaction mixture under inert atmosphere and vigurous mechanical stirring. In the case of magnetite preparation, the inert atmosphere contributed to avoiding the formation of the maghemite phase,  $\gamma\text{-Fe}_2\text{O}_3$ . The metallic ions:oleic acid molar ratio was 1:0.0965. The reaction mixtures were heated at 90 °C, for 30 min and then the precipitation agent was added [14]. The reaction mixtures were heated again at 90°C, for 2.5 h. Cobalt ferrite precipitate was aging at 60°C, for 20 h. The black solid precipitates were filtered off and intensively washed with water and ethanol [11].

The ferrite nanopowders were characterized by wide-angle X-ray diffraction, FTIR spectroscopy, transmission electron microscopy and magnetic measurements at room temperature.

The wide-angle XRD patterns of magnetite and cobalt ferrite nanoparticles (Fig.II.9 și Fig.II.10) obtained in presence of oleic acid showed the formation of the inverse spinel structure with cubic symmetry (spacegroup  $\text{Fd}\bar{3}\text{m}$ ), matching with ICDD 79-0418 and ICDD 22-1086.

The average crystallite size was 8 nm for magnetite, smaller value than for cobalt ferrite, 15 nm, and *unit cell parameter, a*, was 8.478 Å for magnetite, higher than for  $\text{CoFe}_2\text{O}_4$ , 8.370 Å .

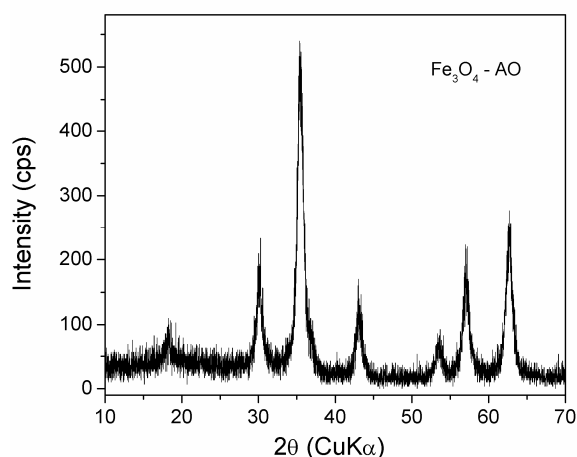


Fig.II.9 Wide-angle XRD pattern of magnetite obtained in the presence of oleic acid

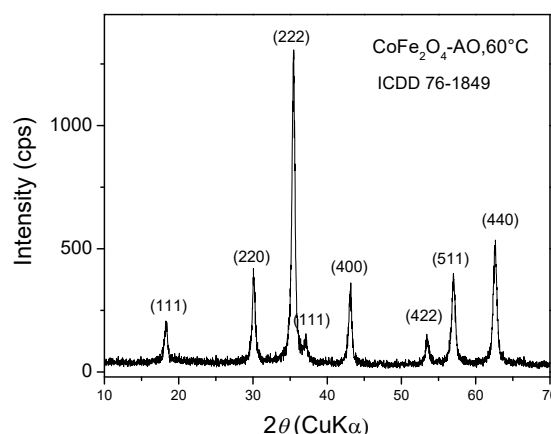


Fig. II.10 Wide-angle XRD pattern of cobalt ferrite obtained in the presence of oleic acid

In the FTIR spectra of magnetite and cobalt ferrite samples obtained in the presence of oleic acid one can observe stronger interactions between magnetite NPs and the capping agent than in the case of cobalt ferrite, being presented the characteristic bands of oleate groups in the range of  $2800\text{-}2900\text{ cm}^{-1}$  (asymmetric and symmetric stretching vibrations of the C-H from the methylene groups), as well as the vibrations of carboxyl groups in the range of  $1350\text{-}1700\text{ cm}^{-1}$ . In both spectra one can observe the intense bands at  $580\text{ cm}^{-1}$  and  $630\text{ cm}^{-1}$  of Fe(II)-O/Co(II)-O și Fe(III)-O bonds in both octahedral and tetrahedral geometries.

The ferrite powders with inverse spinel structure synthesized in the presence of oleic acid were investigated by SEM and TEM. In Fig.II.12 it can be observed that the magnetite present small spherical nanoparticles with the tendency to interact each other through magnetic forces and form spherical agglomerates. The TEM investigation of cobalt ferrite nanopowder (Fig.II.13) showed the formation of polyhedral NPs with narrow size distribution and an average dimension of  $12 \pm 2.5\text{ nm}$  (Fig.II.13 inset).

The magnetic behavior of synthesized ferrite samples was evaluated at room temperature.  $\text{Fe}_3\text{O}_4$  sample exhibited a typical superparamagnetic behavior, while  $\text{CoFe}_2\text{O}_4$  presented ferromagnetic properties, the magnetization curve having a hysteresis loop (Fig.II.14)), which corresponds to a remnant magnetization and coercivity of  $12.63\text{ emu/g}$  and  $369.5\text{ Oe}$ , respectively.  $\text{CoFe}_2\text{O}_4$  did not reach the saturation at applied magnetic field of  $\pm 10\text{ kOe}$ .

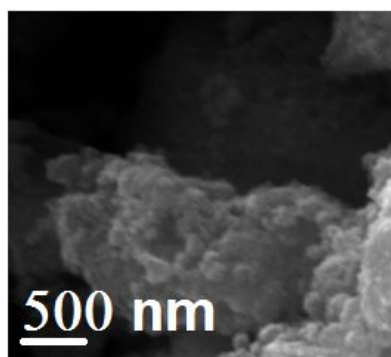


Fig.II.12 SEM image of magnetite powders obtained in the presence of oleic acid

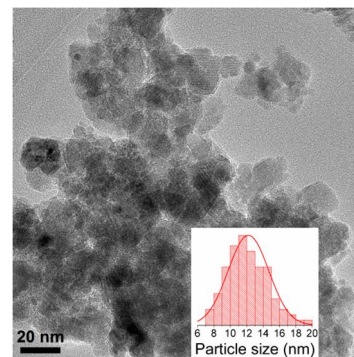


Fig.II.13 TEM image of  $\text{CoFe}_2\text{O}_4$  NPs and their size distribution (inset)

The calculated saturation magnetization values were  $57.10\text{ emu/g}$  for  $\text{Fe}_3\text{O}_4$  and  $52.33\text{ emu/g}$  for  $\text{CoFe}_2\text{O}_4$ , respectively. As it was expected, the saturation magnetization values were

lower than for the bulk  $\text{Fe}_3\text{O}_4$  [12] and  $\text{CoFe}_2\text{O}_4$  due to nanosized particles. It is well known that the loss of the saturation magnetization is due to the small particle surface effect (spin canting effect) and the presence of magnetic dead layer on the small particles surface [15].

The superparamagnetic behavior is related to magneto-crystalline anisotropy that is determined from spin-orbital coupling strength. The superparamagnetic state of  $\text{CoFe}_2\text{O}_4$  is difficult to obtain because among spinel ferrites, it has the highest value of spin-orbital coupling and anisotropy constant and its superparamagnetic critical particle size is very small, much lower than for magnetite [16].

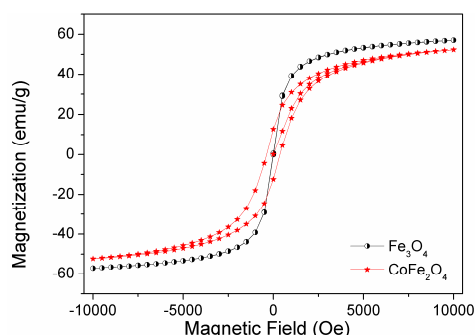


Fig.II.14 Room temperature magnetization curves of ferrite samples.

It was reported for cobalt ferrite NPs with a diameter around 25 nm, prepared by coprecipitation in the presence of oleic acid, lower values for saturation magnetization and coercivity of 46.2 emu/g and 147 Oe, respectively [1] than for our cobalt ferrite sample [11]. The determination of specific surface area values for spinel oxide nanopowders by BET method, determined in range of partial pressure,  $p/p_0$ , 0,01-0,25, revealed a higher value for  $\text{CoFe}_2\text{O}_4$  (119  $\text{m}^2/\text{g}$ ) than for  $\text{Fe}_3\text{O}_4$  (21  $\text{m}^2/\text{g}$ ).

### II.3.3 Synthesis of magnetite in the presence of CTAB

The preparation of magnetite nanoparticles in the presence of CTAB was performed using different precursors. Iron (II) dichloride or iron (II) sulfate were used as Fe (II) precursor.  $\text{FeCl}_2$  was added in 20% excess in comparison with the magnetite stoichiometry, because is more unstable at oxidation than iron (II) sulfate. As  $\text{Fe}^{3+}$  source was used iron trichloride in both cases.

The preparation magnetite NPs from iron dichloride and iron trichloride was carried out by “one-step method”, magnetite nanoparticles were not isolated before their coating with mesoporous MCM-41-type silica layer. In this chapter, only the preparation of magnetite NPs is presented. 2.5 mL and 3.5 mL of 0.5 M aqueous solutions of iron dichloride and iron trichloride, respectively, were added to 54 mL water containing 1.2 g CTAB under mechanical stirring. To avoid the formation of the maghemite phase,  $\text{FeCl}_2$  was added in 20% excess in comparison with the magnetite stoichiometry. Then, 8 mL of 25% (wt.) concentrated aqueous ammonia solution was poured into the reaction mixture at room temperature and a black precipitate was formed [11].

The wide-angle XRD patterns demonstrated the formation of the magnetite phase with inverse spinel crystalline structure and cubic symmetry (space group  $\text{Fd}\bar{3}\text{m}$ ), matching with ICDD 79-0418.

Another synthesis of magnetite NPs using CTAB was performed by using iron (II) sulfate and iron trichloride. In the first step, magnetite nanopowder was synthesized and isolated and in the second step, magnetite NPs were coated with MCM-41-type mesoporous silica.  $\text{Fe}_3\text{O}_4$  were obtained in the presence of CTAB through coprecipitation method using  $\text{FeCl}_3$  and  $\text{FeSO}_4$ . To a solution prepared by dissolution of 2.73 g CTAB in 60 mL ultrapure water, 18 mL 0.5 M  $\text{FeCl}_3$  aqueous solution and 24 mL 0.25 M  $\text{FeSO}_4$  were added under mechanical stirring and inert atmosphere, at 40 °C. After 1 h, 20 mL of 25% (wt.) aqueous ammonia solution were poured into the solution containing  $\text{Fe}^{2+}$  and  $\text{Fe}^{3+}$  ions under argon atmosphere. The reaction mixture was stirred for 1 h at 40 °C and the resulting nanoparticles were isolated and washed with water and ethanol by magnetic decantation [10].

The wide-angle XRD pattern of  $\text{Fe}_3\text{O}_4$  NP shows the formation of the cubic magnetite phase with inverse spinel structure (ICDD 76-1849) as the only crystalline phase (Fig.II.15). The

unit cell parameter for magnetite phase computed from all diffraction peaks was 0.836 nm and correspond to the value obtained from N<sub>2</sub> adsorption-desorption isotherm. The crystallite size of 11 nm was calculated using Rigaku PDXL software based on Scherrer's equation from all Bragg reflections for magnetite. The magnetite NP's specific surface area obtained from N<sub>2</sub> adsorption-desorption isotherm is 67,4 m<sup>2</sup>/g [10].

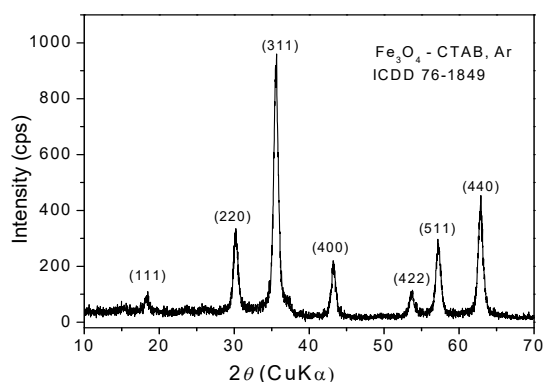


Fig.II.15 Wide-angle XRD pattern of magnetite powder obtained in the presence of CTAB

The morphology of the synthesized powder was investigated through SEM analysis. The Fe<sub>3</sub>O<sub>4</sub> consists of spherical particles with nanometric dimensions, which tend to form spherical agglomerates with a diameter in the range of 50-80 nm (Fig.II.17 (A)) [10].

Magnetite sample synthesized in the presence of CTAB showed typical superparamagnetic behavior at room temperature (Fig.II.18), demonstrating the nanosize dimension of particles. The saturation magnetization value of magnetite NPs calculated by fitting the magnetization data with a Langevin function is lower than for the bulk material being 59.81 emu/g. It can be noticed that the magnetization did not reach saturation at the maximum value of applied magnetic field [10].

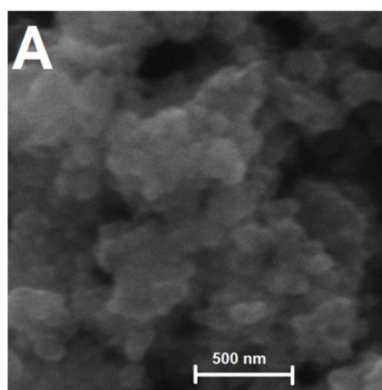


Fig.II.17 SEM image of Fe<sub>3</sub>O<sub>4</sub>

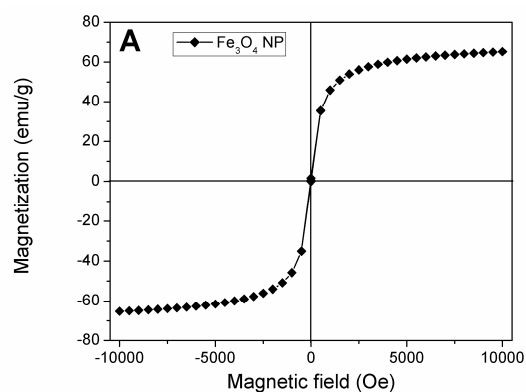


Fig.II.18 Magnetization curve versus applied field at room temperature for Fe<sub>3</sub>O<sub>4</sub> NPs synthesized in the presence of CTAB

#### II.4 Encapsulation of ferrite nanoparticles in mesoporous silica

Magnetic nanoparticles can be coated with organic substances (polymers or surfactants) [18-22], inorganic materials (silica [23], carbon [24], precious metals such as gold or silver [25-27]), or a layer of oxide that is formed through an oxidation process [28]. A special case is core-shell composite materials, in which the magnetite nanoparticles are dispersed or coated in or with a matrix of polymer, silica or carbon. By coating the magnetic nanoparticles and because of the protective coating and they can form stable colloidal solution. Among the methods for the

protection of magnetic nanoparticles, the mesoporous silica coating with magnetite-silica composite materials formation was applied during the PhD studies.

Mesoporous magnetic composites based on cobalt ferrite and magnetite coated with MCM-41 type silica with an ordered hexagonal pore network were synthesized and characterized. In the literature, studies have been reported on the preparation of mesoporous magnetic composites based on magnetite-silica [36,37].

#### **II.4.1 Synthesis and characterization of magnetic composite materials**

For the synthesis of ferrite-silica mesoporous composite materials, magnetic nanoparticles with inverse spinel structure and cubic symmetry obtained by the coprecipitation method using CTAB as surfactant and magnetite and cobalt-ferrite nanoparticles with a spinel structure that were also prepared in aqueous solution, by coprecipitation method, but using oleic acid as stabilizer.

Magnetite and cobalt ferrite nanoparticles prepared in aqueous solution by the coprecipitation method, using oleic acid as stabilizer, and metallic chlorides as precursors.

In order to encapsulate the magnetic nanoparticles in MCM-41-type mesoporous silica matrix, two approaches were used: one pot for the preparation of Fe<sub>3</sub>O<sub>4</sub>-MCM-41 composite material without isolation of magnetite nanoparticles and two steps procedure, in which magnetite nanoparticles or cobalt ferrite were isolated, then dispersed in chloroform and coated with mesoporous silica. In both cases, MCM-41 silica coatings were obtained by the sol-gel method, assisted by hydrothermal treatment [11].

For MCM-41 silica coating of magnetite nanoparticles by the *one-step method*, magnetite NP were prepared in the presence of CTAB without isolation and then the formed NPs were encapsulated into the silica matrix by dropping the silica precursor, tetraethylortosilicate, into the suspension of magnetite NPs. The reaction mixture was mechanically stirred at 40 °C for 24 h followed by a hydrothermal treatment carried out at 100 °C for 24 hours. The formed precipitate was isolated by magnetic separation and washed with water and ethanol to remove the surfactant molecules. The sample was dried at room temperature, calcined at 550 °C for 5h for complete removal of the surfactant and labeled as Fe<sub>3</sub>O<sub>4</sub>-MCM(A) [11].

For the preparation of Fe<sub>3</sub>O<sub>4</sub>-MCM-41 and CoFe<sub>2</sub>O<sub>4</sub>-MCM-41 composites in two steps, magnetite, Fe<sub>3</sub>O<sub>4</sub> and cobalt ferrite CoFe<sub>2</sub>O<sub>4</sub> nanoparticles prepared in the presence of oleic acid were used. 0.045 g of isolated magnetic NPs, Fe<sub>3</sub>O<sub>4</sub> or CoFe<sub>2</sub>O<sub>4</sub>, capped with oleic acid, were dispersed into 2.5 mL of chloroform in an ultrasonic bath. The obtained suspension was added to 60 mL distilled water containing 1.2 g CTAB. The reaction mixtures were kept at 60 °C for 10 min. into the ultrasonic bath for the chloroform evaporation, which contributes also to a good dispersion of the magnetic NPs. Then, concentrated ammonia aqueous solution (3 mL) was poured into the reaction mixtures, followed by the addition of 2.95 mL TEOS. The reaction mixtures were mechanically stirred at 40 °C, 2 4h and then hydrothermally treated at 100 °C for 24 hours. The solids were isolated by magnetic separation and washed with water and ethanol to remove the surfactant molecules. The samples were dried at room temperature and then calcined at 550 °C for 5 hours to completely remove the structure directing agent. The samples were labeled Fe<sub>3</sub>O<sub>4</sub>-MCM(B) and CoFe<sub>2</sub>O<sub>4</sub>-MCM [11].

The wide-angle XRD patterns proved the preservation of ferrite NPs structure and the formation of amorphous silica phase (Fig.II.21 c, d și e), while small-angle XRD patterns demonstrated the formation of mesostructured silica shell, presenting the characteristic Bragg reflections (100), (110) and (200) of MCM-41 material (Fig.II.22).

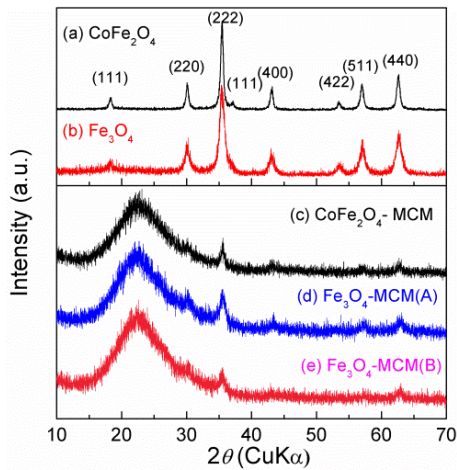


Fig.II.21 Wide-angle XRD patterns of ferrite NPs (a and b) and composite samples (c-e)

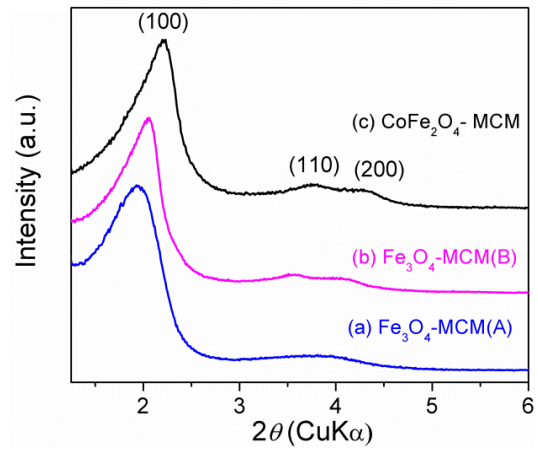


Fig.II.22 Small-angle XRD patterns of magnetic composites

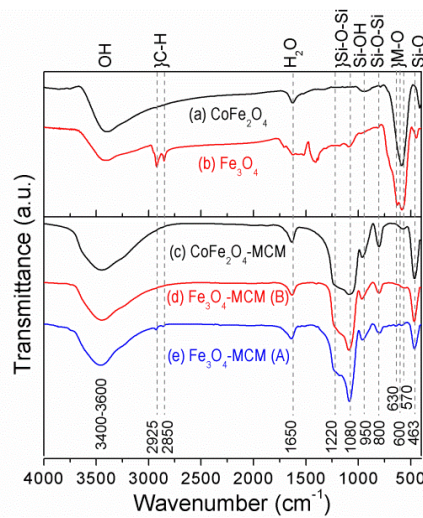


Fig.II.23 FTIR spectra of ferrite NPs (a and b) and magnetic composite samples (c-e)

In the FTIR spectra of composite samples (Fig.II.23), one can observe the characteristic vibrations of silica matrix,  $\nu_{\text{as,s}}(\text{Si-O-Si}) = 1080$  and  $800 \text{ cm}^{-1}$ ,  $\nu_{\text{as}}(\text{Si-OH}) = 950 \text{ cm}^{-1}$ ;  $\delta(\text{Si-O}) = 463 \text{ cm}^{-1}$ , the bands of adsorbed water molecules at  $1650 \text{ cm}^{-1}$ , the large stretching band of OH groups in the range of  $3400\text{-}3600 \text{ cm}^{-1}$ , as well as the stretching vibration of M-O at  $570 \text{ cm}^{-1}$  and  $630 \text{ cm}^{-1}$  for  $\text{Fe}_3\text{O}_4$  and  $600 \text{ cm}^{-1}$  for  $\text{CoFe}_2\text{O}_4$  (Fig. II. 23 c, d, e). The presence of the silica vibrations in the FTIR spectra of all composites demonstrated the encapsulation of ferrite NPs in the silica matrix. In the FTIR spectrum of  $\text{Fe}_3\text{O}_4$  sample it can be also noticed the vibrations of oleate groups (Fig. II.23 b) as result of stronger interactions between magnetite NPs and the capping agent than in the case of cobalt ferrite (Fig.II.23 a).

Table II.2 lists the textural properties (the specific surface area,  $S_{\text{BET}}$ , the volume of pores smaller than  $10 \text{ nm}$ ,  $V_p$ , and the average pore size,  $d_{\text{BJH}}$  calculated using the Barrett Joyner Halenda model), the saturation magnetization values, as well as the ferrite NPs content in the prepared composites determined by ICP-MS analysis.

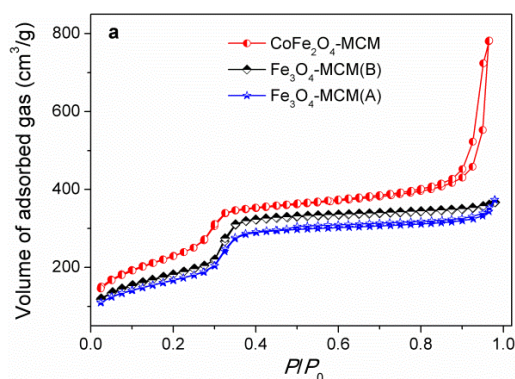


Fig. II.24 a  $N_2$  adsorption-desorption isotherms of magnetic composite samples

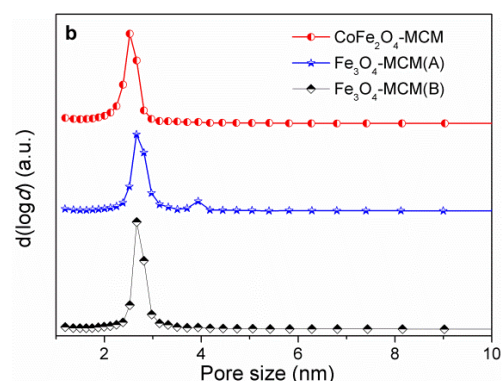


Fig.II.24 b Pore size distribution curves of magnetic composite samples calculated using BJH model for ferrite-silica mesoporous composites

The magnetic composites present type IV nitrogen adsorption-desorption isotherms characteristic for MCM-41 materials (Fig.II.24 a). All the composites have relatively high specific surface area and mesopores volume values that are necessary in drug delivery applications (Table II.2). The highest value of specific surface area was determined for  $CoFe_2O_4$ -MCM sample, whose isotherm presents also a fraction of macropores that corresponds with the sharp increase of adsorbed gas volume at relative pressure,  $P/P_0$ , higher than 0.9 corresponding to magnetic interparticle voids. The pore size distribution curve for all samples is unimodal and the average pore size, ranging between 2.52 nm for  $CoFe_2O_4$ -MCM and 2.67 nm for the  $Fe_3O_4$ -MCM(B), is characteristic for MCM-41-type materials (Fig. II.24 b).

The TEM investigation of magnetic composites proved the encapsulation of ferrite NPs into an ordered MCM-41 mesoporous silica matrix. The  $Fe_3O_4$ -MCM(A) sample obtained by one-pot approach has small magnetite NPs, with narrow size distribution and an average size of  $6.5 \pm 1.5$  nm, dispersed in mesoporous silica matrix (Fig.II.25 a).  $Fe_3O_4$ -MCM(B) sample showed at TEM investigation that magnetite NPs are embedded in the mesostructured silica matrix having narrow size distribution and an average size of  $7 \pm 1.7$  nm (Fig.II.25 b) [11].

Table II.2 Properties of magnetic composites

Composite samples	$S_{BET}$ ( $m^2/g$ )	$V_p$ ( $d_{por} < 10$ nm) ( $cm^3/g$ )	$d_{BJH}$ (nm)	$M_s$ (emu/g)	Content of ferrite NPs (% wt.)
$Fe_3O_4$ -MCM(A)	612	0.51	2.66	3.77	5.64
$Fe_3O_4$ -MCM(B)	664	0.58	2.67	1.79	3.77
$CoFe_2O_4$ -MCM	784	0.66	2.52	1.26	3.10

$CoFe_2O_4$  NPs with a tendency to interact each other to form agglomerates of two or three nanoparticles are embedded into the mesoporous silica matrix forming spherical particles with an average diameter of 160 nm and an ordered pore array, in agreement with the small-angle XRD pattern (Fig.II.25 c, d). Some smaller particles with an average size of 27 nm are also observed.

The magnetic behavior of all composites was measured by VSM at room temperature. There was no hysteresis detected for any composite samples containing  $Fe_3O_4$ , indicating superparamagnetic properties, while  $CoFe_2O_4$ -MCM material showed a ferrimagnetic behavior (Fig.II.26). The remnant magnetization and coercivity values of silica coated cobalt ferrite were 0.38 emu/g and 427 Oe, respectively.

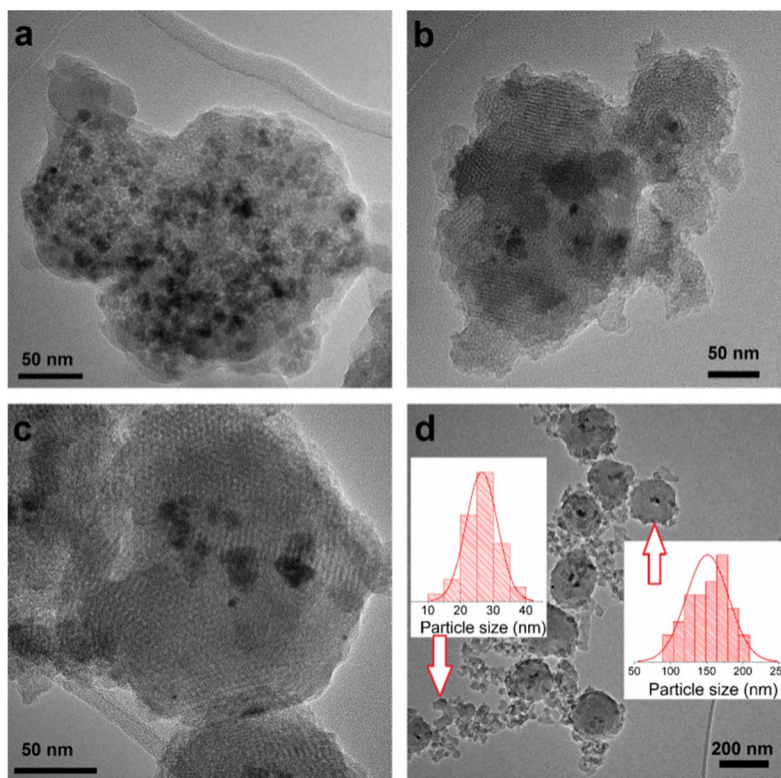


Fig. II.25 TEM images of magnetic composites:  $\text{Fe}_3\text{O}_4$ -MCM(A) sample (a),  $\text{Fe}_3\text{O}_4$ -MCM(B) material (b) and  $\text{CoFe}_2\text{O}_4$ -MCM sample (c and d). Inset, the particle size distribution of  $\text{CoFe}_2\text{O}_4$ -MCM.

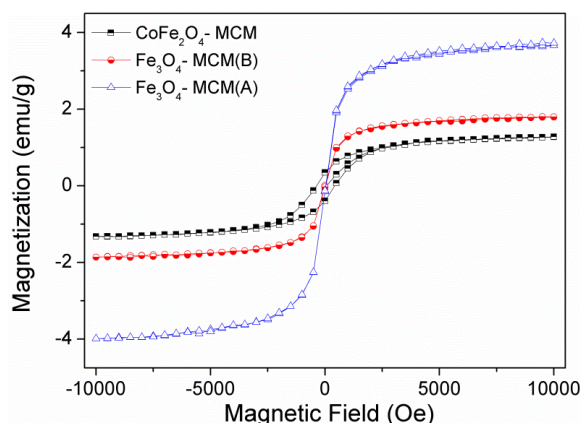


Fig.II.26 Magnetization curves of magnetic composite materials

The saturation magnetization value of 1.26 emu/g for synthesized  $\text{CoFe}_2\text{O}_4$ -MCM-41 composite with 3.10% (wt.) magnetic phase is higher than 0.6 emu/g reported in literature for the composite obtained by impregnation of mesoporous silica with cobalt ferrite nanoparticles having a spinel phase content of 6.4% (wt.) [39].

It was recently proved based on Mössbauer spectra that amorphous silica coated  $\text{CoFe}_2\text{O}_4$  particles with the crystallite size in the range of 2.2–4.3 nm were not superparamagnetic, but were paramagnetic, this property being specific for magnetic nanoparticles isolated by another nonmagnetic material [40].

#### II.4.1.1 Studies on cellular toxicity of magnetic composite materials

For the cytotoxicity assays of magnetic mesoporous composite samples was used OK cell line (adherent epithelial opossum kidney cells). The OK cell line was exposed 48 h to 50, 100 and 200  $\mu\text{g}/\text{mL}$   $\text{Fe}_3\text{O}_4$ -MCM(B) și  $\text{CoFe}_2\text{O}_4$ -MCM magnetic composites nanoparticles as well as  $\text{CoFe}_2\text{O}_4$  NPs. The mitochondrial activity of cells (mitochondria is a cytoplasmic organism made

up of proteins, lipids and enzymes that provide energy for the cell) was evaluated through the reduction of a tetrazolium-type compound to a formazan product in metabolically active cells [41,42]. The toxicity was quantified by measuring the absorbance of the samples at 490 nm.

The absorbance of the formazan derivative that is produced in an active cell is directly proportional with the number of viable cells. The cellular proliferation was not affected even at high concentrations (Fig.II.27) that were sometimes reported as toxic in the literature. For example, it was reported that  $\text{CoFe}_2\text{O}_4$  NPs are cytotoxic to human pancreatic and ovarian cancer cells at concentration higher than  $0.95 \mu\text{m}/\text{mL}$  [43], while cell viability assays showed low toxicity of  $\text{CoFe}_2\text{O}_4$  NPs of 4 nm on lung cancer cells in the concentration range of 0.2-0.8 mg/mL [44].

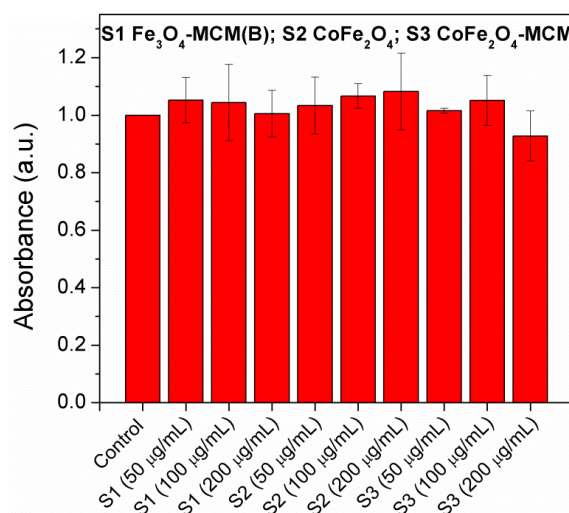


Fig. II.27 Toxicity after 48 h exposure to magnetic samples.

#### II.4.2 Synthesis and characterization of $\text{Fe}_3\text{O}_4@MCM-41$ magnetic composites in the presence of CTAB

$\text{Fe}_3\text{O}_4@MCM-41$  nanocomposites were also synthesized, in a two-step procedure, but the magnetite nanoparticles were synthesized by the co-precipitation method using precursors, iron (III) chloride,  $\text{FeCl}_3 \cdot 6\text{H}_2\text{O}$  0.5 M and iron (II) sulphate, 0.25 M  $\text{FeSO}_4 \cdot 7\text{H}_2\text{O}$ , in the presence of CTAB at  $40^\circ\text{C}$  in an inert atmosphere by precipitation with concentrated ammonia solution (25% wt.). The magnetite nanoparticles were washed with a mixture of water and alcohol (vol.) 50:50 and recovered by magnetic decantation.

For coating  $\text{Fe}_3\text{O}_4$  NP with MCM-41 type silica, 0.046 g  $\text{Fe}_3\text{O}_4$  NP (0.2 mmol) were dispersed by ultrasonic treatment into a solution containing 0.600 g CTAB (1.64 mmol) and 2.5 mL ammonia in 30 mL water. 2.5 mL TEOS (11.2 mmol) were added and the reaction mixture was mechanically stirred at  $40^\circ\text{C}$  for 24 h. The reaction mixture was hydrothermally treated at  $150^\circ\text{C}$  for 24 h, followed by the solid separation and surfactant removal through extraction in a 2% (wt) ammonium nitrate alcoholic solution. The sample was labeled  $\text{Fe}_3\text{O}_4@MCM-41E$ [10].

The wide-angle XRD pattern (Fig.II.28) demonstrated that magnetite nanoparticles were encapsulated in MCM-41 type silica. For the  $\text{Fe}_3\text{O}_4@MCM-41E$  sample an additional broad peak between  $15-35^\circ 2\theta$ , corresponding to amorphous silica phase formation can be noticed.

The crystallite size of magnetite phase (11 nm) was not altered after the silica coating procedure or the composite extraction [10].

The small-angle diffraction pattern (Fig.II.29) of  $\text{Fe}_3\text{O}_4@MCM-41$  composite material presents three characteristic peaks, indexed as the (100), (110) and (200) Bragg reflections of the hexagonal space group  $P6m$ [10].

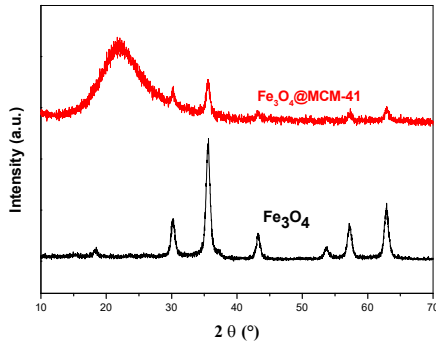


Fig.II.28 Wide-angle XRD patterns of Fe<sub>3</sub>O<sub>4</sub> NP and Fe<sub>3</sub>O<sub>4</sub>-MCM-41E silica-magnetite composites

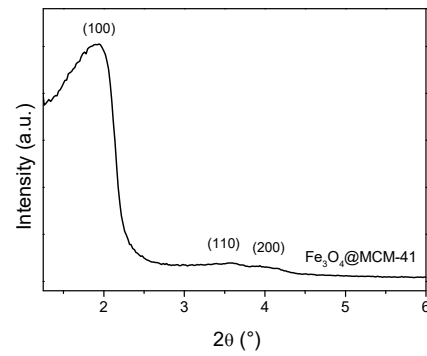


Fig.II.29 Small-angle XRD pattern of Fe<sub>3</sub>O<sub>4</sub>@MCM-41E

The nitrogen adsorption-desorption isotherms (Fig.II.30) for Fe<sub>3</sub>O<sub>4</sub>@MCM-41E composite material is type IV, characteristic for mesoporous materials [45] and presents H1-type hysteresis, characteristic for independent pores with hexagonal arrangement. The pore size distribution curve is calculated from the desorption branch of the isotherm by Barrett Joyner Halenda (BJH) method [46]. This approach is suitable for non-intersecting mesopores as the case of MCM-41-type materials.

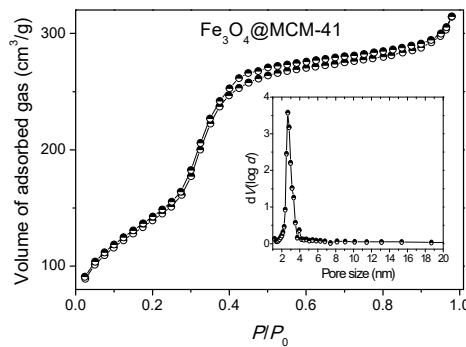


Fig.II.30 N<sub>2</sub> adsorption–desorption isotherm and the corresponding pore size distribution curve for Fe<sub>3</sub>O<sub>4</sub>@MCM-41E

Table II.3 Unit cell parameter, specific surface area, total pore volume and average pore diameter values for the Fe<sub>3</sub>O<sub>4</sub> nanoparticles and Fe<sub>3</sub>O<sub>4</sub>@MCM-41E magnetite-silica material

Sample	$a_0$ (nm)*	$S_{BET}$ (m <sup>2</sup> /g)	$V_{pore}$ (cm <sup>3</sup> /g)	$d_{pore}$ (nm)
Fe <sub>3</sub> O <sub>4</sub>	0.836	67.4	-	-
Fe <sub>3</sub> O <sub>4</sub> @MCM-41E	5.10	515	0.46	2.67

\* $a_0 = 2d_{100} / \sqrt{3}$  for mesoporous silica with hexagonal pore array

Unit cell parameter,  $a_0$ , specific surface area,  $S_{BET}$ , total pore volume  $V_{pore}$ , and average pore diameter values,  $d_{pore}$ , for the Fe<sub>3</sub>O<sub>4</sub> nanoparticles and Fe<sub>3</sub>O<sub>4</sub>@MCM-41E magnetite-silica material are presented in Table II.3.

The morphology of the synthesized materials was investigated through SEM analyses (Fig. II.17 (A) și II.31 B,C). The Fe<sub>3</sub>O<sub>4</sub>@MCM-41E composite (Fig.II.31 B) consists of large spherical particles, polydisperse in size, with a diameter between 200 nm and 500 nm. A very good dispersion of the magnetite nanoparticles (bright spots) into the MCM-41 framework can be noticed for Fe<sub>3</sub>O<sub>4</sub>@MCM-41E (Fig.31 B) in the back scatter electrons (BSE) detection mode from SEM image [10]. The EDX map of Fe<sub>3</sub>O<sub>4</sub>@MCM-41E (Fig.II.31 C) also shows a good dispersion of Fe<sub>3</sub>O<sub>4</sub> nanoparticles in the silica matrix. The ratio Fe/Si was found using EDX

quantitative analyses in at least five different areas of each sample (Table II.4) and it is lower than the initial ratio used in the synthesis. For  $\text{Fe}_3\text{O}_4@\text{MCM-41}$ , the content of magnetite phase computed from EDX analysis was 7.2% (wt) [10].

FT-IR spectroscopy was used to assess the various chemical bonds present in the obtained materials (Fig.II.32). The characteristic stretching vibrations associated with Fe-O bonds for the  $\text{Fe}_3\text{O}_4$  NPs are observed at  $450\text{ cm}^{-1}$ ,  $580\text{ cm}^{-1}$  and  $630\text{ cm}^{-1}$  and correspond to the Fe(II) and Fe(III) ions in both octahedral and tetrahedral geometries [7]. These bands can be also noticed in the silica-magnetite materials, proving the successful incorporation of magnetite in mesoporous silica matrix, even though the  $450\text{ cm}^{-1}$  Fe-O in octahedral geometry is superimposed with the  $465\text{ cm}^{-1}$  Si-O bending vibration.

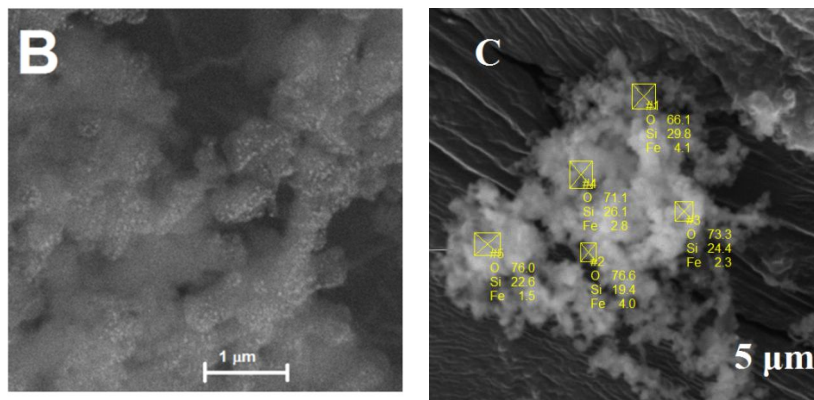


Fig.II.31 SEM images of  $\text{Fe}_3\text{O}_4@\text{MCM-41E}$  and  $\text{Fe}_3\text{O}_4@\text{MCM-41E(C)}$  with elements distribution

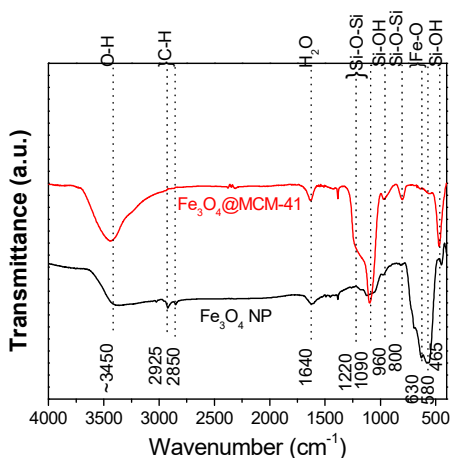


Fig. II.32 FT-IR spectra of magnetite nanoparticles and magnetite-silica composite

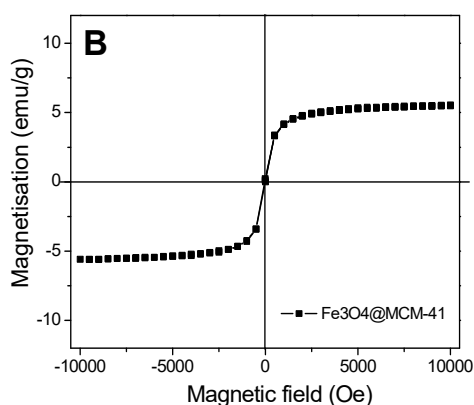


Fig.II.33 Magnetization versus applied field curves for  $\text{Fe}_3\text{O}_4@\text{MCM-41}$  at room temperature

The presence of silica in the composite materials is indicated by its characteristic vibrations: Si-O-Si asymmetric stretching at  $\sim 1090\text{ cm}^{-1}$ , Si-O-Si symmetric stretching at  $\sim 800\text{ cm}^{-1}$  and Si-OH deformation vibrations at  $\sim 960\text{ cm}^{-1}$ . Samples contain physisorbed water and surface hydroxyl groups, as evidenced by the  $1640\text{ cm}^{-1}$  water bending vibration and the broad  $3450\text{ cm}^{-1}$  O-H stretching vibration, respectively. Lastly, the existence of surfactant molecules for  $\text{Fe}_3\text{O}_4$  NP can be inferred through the C-H stretching bands between  $2850\text{--}2925\text{ cm}^{-1}$  and the C-C and C-N vibrations in the  $1200\text{--}1500\text{ cm}^{-1}$  range [10].

The magnetic susceptibility measurements at room temperature of both magnetite NPs and magnetite-mesoporous silica material show a typical superparamagnetic behavior, with anhysteretic behavior (Fig.II.33). The magnetization ( $M$ ) versus applied magnetic field ( $H$ ) curves present a sharp increase in magnetization between  $-3000$  and  $3000\text{ G}$  for both samples,

reaching saturation at around 4000 G. This behavior is characteristic for magnetite [36] and demonstrates the preservation of Fe<sub>3</sub>O<sub>4</sub> phase in the nanocomposite samples. A high saturation magnetization is desired for the magnetite-silica composite for targeted drug delivery or catalysis. As expected, the saturation magnetization of Fe<sub>3</sub>O<sub>4</sub> nanoparticles (59.8 emu/g) is lower than that of bulk magnetite (~95 emu/g) [12] due to the nanometer size of Fe<sub>3</sub>O<sub>4</sub> NP [10].

Table II.4 Saturation magnetization ( $M_s$ ), magnetic susceptibility ( $\chi_g$ ) and Fe<sub>3</sub>O<sub>4</sub> content computed from magnetic measurements and EDX analysis

Sample	$M_s$ (emu/g)	$\chi_g \cdot 10^6$	Fe <sub>3</sub> O <sub>4</sub> content from $M_s$ (% wt.)	Fe <sub>3</sub> O <sub>4</sub> content from EDX (% wt.)
Fe <sub>3</sub> O <sub>4</sub> NP	59.81	14.00	-	-
Fe <sub>3</sub> O <sub>4</sub> @MCM-41E	5.24	1.52	8.7	7.2

From table II.4, one can observed that the magnetic susceptibility and saturation magnetization values are lower for Fe<sub>3</sub>O<sub>4</sub>@MCM-41E sample than for the magnetite nanoparticles due to the formation of the non-magnetic mesoporous silica layer [10].

## II.5 Antibiotics delivery systems

### II.5.1 Synthesis and characterization silica-titania mesoporous composite materials

The mesostructured silica–titania composites with up to 30% (mol) titania and 1D pore array were obtained by sol–gel method assisted by hydrothermal treatment, using tetraethyl orthosilicate and titanium oxydichloride as silica and titania precursor, respectively, in the presence of triblock copolymer, Pluronic P123, as structure directing agent. The silica–titania supports for various active pharmaceutical ingredients were compared with a SBA–15-type silica. Titanium oxydichloride used as titania precursor was freshly prepared from titanium tetraisopropoxide and concentrated hydrochloric acid according literature data [47].

The small-angle XRD patterns (Fig.II.35) of all synthesized supports present three characteristic diffraction peaks corresponding to (100), (110) and (200) Bragg reflections of SBA-15-type materials, proving the formation of an ordered hexagonal pore array for all samples. The increase of titanium content led to the enlargement of  $a_0$  lattice parameter (Table II.5) [48]. The wide-angle XRD patterns (Fig.II.36) of silica-titania composite samples show the diffraction peaks characteristic for the anatase phase and the broad signal corresponding to the amorphous silica. The only exception is the Ti4.5SBA-15 sample for which the diffraction peaks of anatase phase are hardly detectable, suggesting that titanium is mostly incorporated into the silica framework, in agreement with literature data [49,50].

The crystallite dimension generally increases with the titanium content, except the values recorded for Ti10SBA-15 and Ti20SBA-15, which are very close (Tabelul II.5) [48].

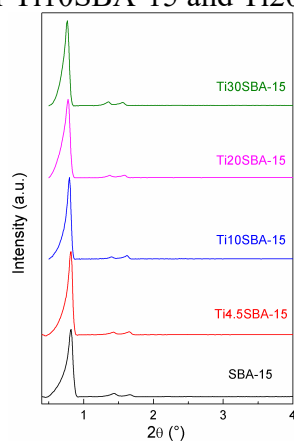


Fig.II.35 Small-angle X-ray diffraction patterns of SBA-15 silica and mesoporous silica-titania composite materials.

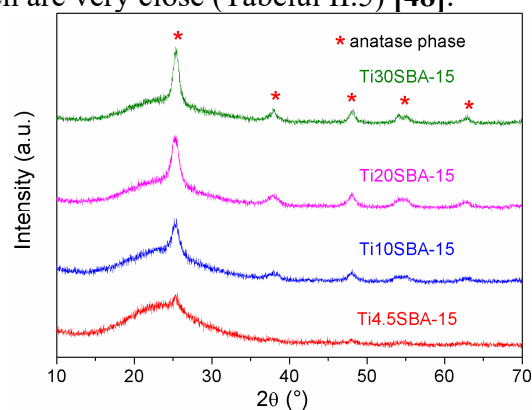


Fig. II.36 Wide-angle X-ray diffraction patterns of mesoporous silica-titania composite materials.

The electron microscopy images of titania-silica supports revealed the formation of fibre or rope-like aggregates characteristic for SBA-15 silica, with a certain degree of ordering (straighter and longer fibres) for Ti10SBA-15 powder (Fig.II.38 b).

The fibres-like arrangement appears more distorted with the increase of titanium content. The EDX elemental mapping shows an even distribution of titanium in the silica framework for all titania-silica composite samples (Fig.II.38 a și Fig.II.39), while crystalline titania nanoparticles are noticed in both SEM and TEM images (Fig. II.38 b, c and d).

All samples present type IV  $N_2$  adsorption/desorption isotherms, characteristic of SBA-15-type materials ((Fig.II.40 a) and unimodal pore size distribution curves (Fig.II.40 b). Larger pore size values were obtained for pristine SBA-15 than for titania-silica samples (Tabelul II.5) suggesting a contraction of the mesoporous framework due to the presence of the titanium dopant. Although a slight increase in the pore size is noticed with increasing titania content, the wall thickness values remains relatively constant, indicating the saturation of the mesostructure in titanium. Notably, the textural properties of the Ti10SBA-15 and Ti20SBA-15 samples, as well as titania crystallite size for both samples are similar, despite of the difference in  $a_0$  lattice parameter [48].

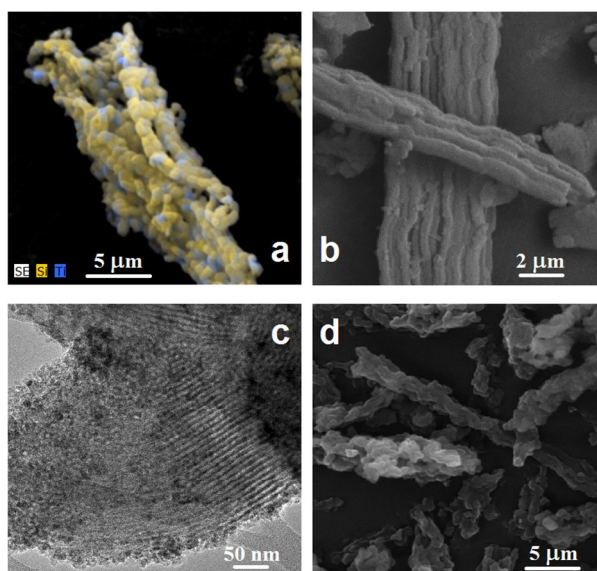


Fig.II.38 Electron microscopy images of titania-silica supports: (a) SEM image of Ti4.5SBA-15 sample with EDX elemental mapping; (b) SEM image of Ti10SBA-15; (c) TEM image of Ti20SBA-15 sample; (d) SEM image of Ti30SBA-15 samples.

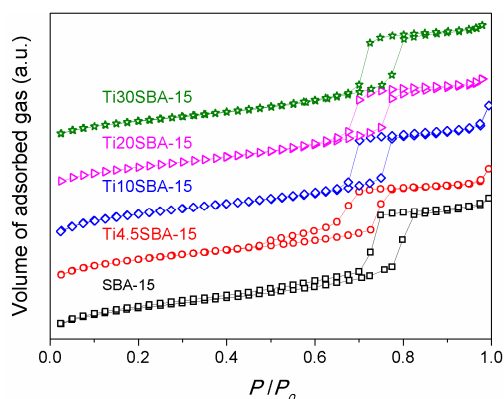


Fig.II.40 a Nitrogen adsorption/desorption isotherms of SBA-15 type silica and mesoporous silica-titania composite materials.

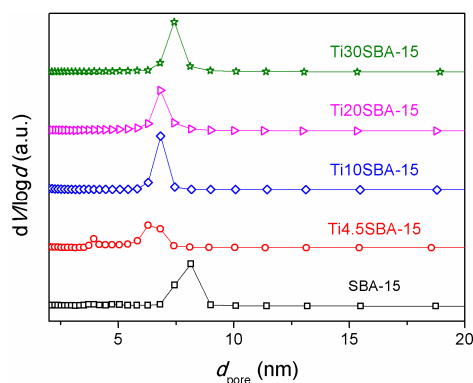


Fig.II.40 b Pore size distribution curves of SBA-15 type silica and mesoporous silica-titania composite materials obtained with BJH model determined from the desorption branch of nitrogen adsorption/desorption isotherms.

Table II.5 Structural and textural parameters of mesoporous silica-titania composites [48]

Sample	Ti content (% mol)	$d_{100}$ (nm)	$a_0$ (nm)	$wt$ (nm)	$S_{BET}$ (m <sup>2</sup> /g)	$d_{BJH}^*$ (nm)	$V_{pt}/V_p^{**}$ (cm <sup>3</sup> /g)	$D_{200}^{***}$ (nm)
SBA-15	0	10.960	12.655	4.515	997	8.14	1.49/1.34	-
Ti4.5SBA-15	4.5	11.005	12.707	6.437	959	6.27	1.29/1.10	12.5
Ti10SBA-15	10	11.170	12.898	6.078	1081	6.82	1.50/1.21	75.9
Ti20SBA-15	20	11.479	13.255	6.445	826	6.82	1.50/1.21	78
Ti30SBA-15	30	11.663	13.468	6.058	742	7.41	1.24/1.14	100

\* pore diameter determined from the desorption branch of isotherms

\*\*  $V_{pt} / V_p$  – total pore volume including mesopores and macropores vs. mesopores volume of pores with diameter smaller than 10 nm

\*\*\* TiO<sub>2</sub> crystallite size computed from (200) diffraction peak ( $2\theta=48^\circ$ ) of anatase phase

### II.5.2 Evaluation of silica-titania mesoporous composite materials in drug delivery systems

The oxytetracycline-loaded materials with a drug content of 25% (wt.) or 33% (wt.) were obtained by incipient wetness impregnation method using a concentrated aqueous solution of antibiotic. In brief, 100 mg mesoporous support was added to the corresponding volume of freshly prepared oxytetracycline hydrochloride aqueous solution with a concentration of 100 mg/mL. The support and antibiotic solution were mixed for homogenization and then the mixture was vacuum dried in dark conditions for 12 h [48].

The pristine SBA-15 silica and silica-titania composite materials loaded with oxytetracycline were characterized by wide-angle XRD, FT-IR spectroscopy and nitrogen adsorption-desorption isotherms. The FTIR spectra of all oxytetracycline-loaded samples evidence the presence of antibiotic into the inorganic matrices. In Fig.II.42 can be noticed FTIR spectra oxytetracycline-loaded materials based on inorganic mesoporous matrix compared with the antibiotic spectrum.

The characteristic vibrations of oxytetracycline are identified in the range of 2850-2950 cm<sup>-1</sup>, ascribed to the methylene groups, 1590-1650 cm<sup>-1</sup>, attributed to the amide groups, and 1310-1410 cm<sup>-1</sup>, assigned to the phenol moieties [54]. The oxytetracycline-mesoporous inorganic matrix were analysed by wide-angle XRD. In the wide-angle XRD patterns of the oxytetracycline-loaded materials with a drug content of 25% (wt.) or 33% (wt.), one can observe no diffraction peaks of the drug, and only those characteristic of anatase phase (Fig.II.44). Correlating the FTIR spectra with the wide-angle XRD patterns, one can conclude that the oxytetracycline molecules were adsorbed into the pores of support in amorphous state [48].

Similar to the supports, all drug-loaded samples exhibit type IV N<sub>2</sub> adsorption/desorption isotherms, but with narrow hysteresis loop (Fig.II.45) indicating that not all the pores are completely filled with drug molecules. However, the samples showed lower porosity than the corresponding carriers, more pronounced in the case of materials containing 33% (wt) drug (Table II.6) and reduced values for both specific surface area and total pore volume. On the other hand, the pore size values decrease for the drug-loaded SBA-15 silica samples, while for the materials containing titania-silica composites they remain almost unchanged. This indicates a different mechanism of the drug hosting into the support mesopores, namely, by adsorption onto the inner pore surface in the case of pristine SBA-15 and a loading that involves the pore clogging being more likely for the titanium-doped silica network. The origin of this opposite behaviour could lay on the different wetting properties of silica and titania-silica composite materials [48].

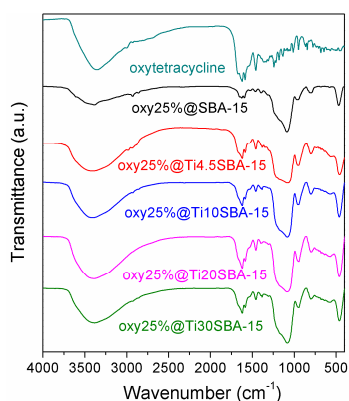


Fig. II.42 FTIR spectra of oxytetracycline-loaded silica-titania mesoporous composites.

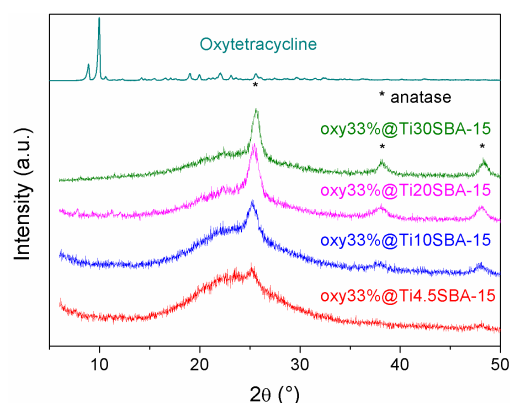


Fig.II.44 Wide-angle XRD patterns of oxytetracycline-loaded samples: with 33% (wt) oxytetracycline.

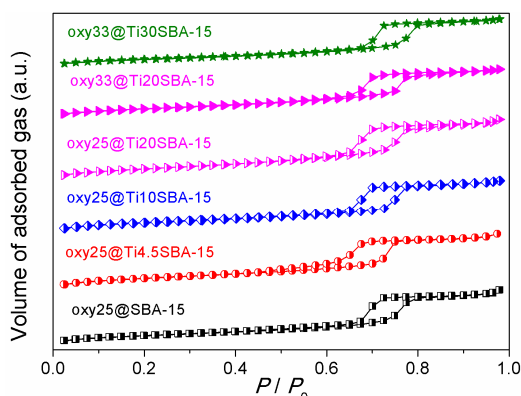


Fig.II.45 Nitrogen adsorption/desorption isotherms of representative oxytetracycline-mesoporous inorganic matrix

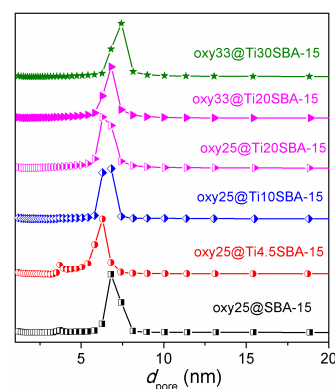


Fig.II.46 Pore size distribution curves of oxytetracycline-mesoporous inorganic matrix.

Table II.6 Textural properties of oxytetracycline-loaded supports [48]

Sample	$S_{\text{BET}}$ (m <sup>2</sup> /g)	$d_{\text{BJH}}^*$ (nm)	$V_{\text{pt}}/V_{\text{p}}^{**}$ (cm <sup>3</sup> /g)
oxy25%@SBA-15	302	6.81	0.5/0.57
oxy25%@Ti4.5SBA-15	333	6.29	0.56/0.51
oxy25%@Ti10SBA-15	337	6.30	0.53/0.48
oxy25%@Ti20SBA-15	353	6.29	0.63/0.57
oxy25%@Ti30SBA-15	314	6.81	0.61/0.68
oxy33%@SBA-15	208	6.28	0.34/0.37
oxy33%@Ti4.5SBA-15	219	6.28	0.36/0.44
oxy33%@Ti10SBA-15	327	6.29	0.48/0.56
oxy33%@Ti20SBA-15	284	6.82	0.47/0.51
oxy33%@Ti30SBA-15	233	7.43	0.45/0.49

\* pore diameter determined from the desorption branch of isotherm; \*\*  $V_{\text{pt}} / V_{\text{p}}$  – total pore volume including mesopores and macropores vs. pore volume calculated for pores with diameter up to 10 nm.

### II.5.2.2 *In vitro* release profiles of oxytetracycline from silica-titania mesoporous composites

The oxytetracycline release experiments were performed in 0.2 M saline phosphate buffer solution (PBS) as simulated body fluid, at 37 °C, under magnetic stirring (150 rpm). An amount of drug-loaded material containing 12.5 mg antibiotic was added to 90 mL PBS. At predetermined time intervals, set amounts of simulated body fluid were withdrawn, diluted and analyzed by UV-Vis spectroscopy to determine the antibiotic release amount on the basis of the previously determined calibration curve.

The release profiles (Fig.II.47 a și b) show a decrease of antibiotic release from inorganic mesoporous supports, which contains crystalline anatase nanoparticles: Ti10SBA-15, Ti20SBA-15 and Ti30SBA-15, while from Ti4.5SBA-15 the profiles are similar with those recorded for the drug-loaded SBA-15 samples, presenting even a higher *burst* effect (Fig.II.48). The crystalline titania, located on the silica surface, positively contribute to the decrease of the drug delivery rate. The lowest sustained antibiotic release rates were noticed for oxy25@Ti10SBA-15 (Fig.II.48 a) and oxy33@Ti10SBA-15 (Fig.II.48 b) samples, an expected performance as the longest fibre-like structures and mesopore channels were observed for Ti10SBA-15 support. The experimental drug release profiles were fitted with a three-parameter theoretical kinetic model.

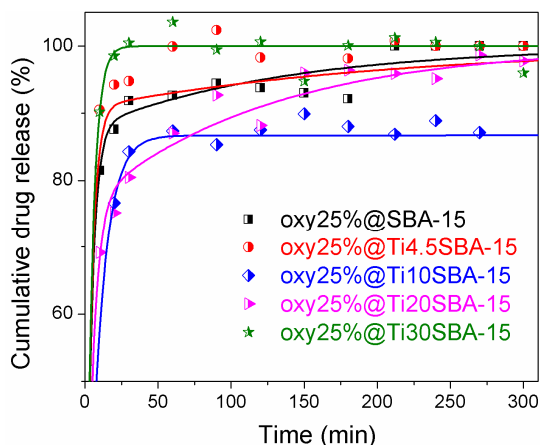


Fig.II.47a Oxytetracycline release profiles for samples containing 25% (wt) drug. Symbols and continuous lines denote experimental and fitted data, respectively.

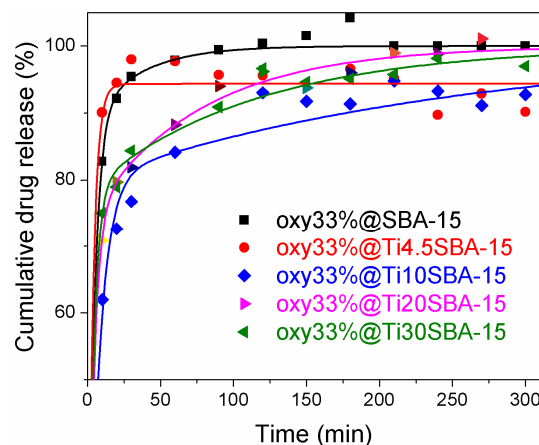


Fig.II.47 b Oxytetracycline release profiles for samples containing 33% (wt) drug. Symbols and continuous lines denote experimental and fitted data, respectively.

#### Equations of the three parameter model

Assuming that the adsorption and desorption processes both follow the first order kinetics, with the rate constants  $k_{on}$  and  $k_{off}$ , respectively, the molecular free enthalpy can be written as:

$$\Delta G = -k_B T \cdot \ln(k_{on}/k_{off})$$

where  $k_B$  represents Boltzman's constant and  $T$ , temperature.

The equation used to fit the experimental release data is given by :

$$\frac{m(t)}{m(0)} = \frac{\lambda_2(k_d - \lambda_2)}{(k_{on} + k_{off})(\lambda_1 - \lambda_2)} (1 - e^{-\lambda_1 t}) + \frac{\lambda_1(\lambda_1 - k_d)}{(k_{on} + k_{off})(\lambda_1 - \lambda_2)} (1 - e^{-\lambda_2 t}),$$

where  $m(t)$  and  $m(0)$  denote the cumulative drug release at time  $t$  and total drug amount and

$$\lambda_{1,2} = \left[ (k_d + k_{on} + k_{off}) \pm \sqrt{(k_d + k_{on} + k_{off})^2 - 4k_s k_{off}} \right] / 2$$

This model assumes that there is an equilibrium between drug molecules adsorbed onto the carrier surface and desorbed molecules inside the mesopores [55-57]. The molecules are transported through the mesochannels into the release medium by diffusion, which is assumed to follow a first order kinetics.

A correlation study between the kinetic release parameters and the textural properties of the carriers has been considered (Tabelul II.8). The correlation coefficients take values between -1 and 1, with values close to  $\pm 1$  denoting either direct or inverse correlation and values close to 0 indicating no correlation. The results show that titanium content is strongly correlated with the unit cell parameter ( $a_0$ ) of mesophase. These two parameters also show an inverse correlation with the free enthalpy  $\Delta G$  for both 25% and 33% drug loadings. Thus increasing the titanium content is a promising strategy to design oxytetracycline delivery systems.

Table II.7 Kinetics release parameters for oxytetracycline-loaded samples

Sample	25% (wt.) oxy			33% (wt.) oxy		
	$\Delta G$ ( $10^{21}$ J)	$k_d$ ( $\text{min}^{-1}$ )	$R^2$	$\Delta G$ ( $10^{21}$ J)	$k_d$ ( $\text{min}^{-1}$ )	$R^2$
SBA-15	8.67	0.249	0.994	10.08	0.228	0.998
Ti4.5SBA-15	9.95	0.257	0.987	12.05	0.293	0.990
Ti10SBA-15	8.03	0.110	0.997	6.25	0.131	0.985
Ti20SBA-15	5.43	0.203	0.982	5.17	0.242	0.995
Ti30SBA-15	6.26	0.086	0.990	5.90	0.262	0.987

Table II.8 Correlation coefficients between the carriers textural and structural parameters and the drug release kinetics parameters.

Parameters	<i>Ti content</i>	$a_0$	<i>wt</i>	$S_{\text{BET}}$	$d_{\text{BJH}}$	$V_p$
$a_0$	0.99	1.0				
$\Delta G$ , 33% oxy	-0.77	-0.81	-0.30	0.41	-0.07	-0.25
$k_d$ , 33% oxy	0.14	0.12	0.16	-0.62	-0.12	-0.67
$\Delta G$ , 25% oxy	-0.83	-0.88	-0.26	0.69	-0.15	-0.13
$k_d$ , 25% oxy	-0.72	-0.69	-0.27	0.27	-0.03	0.20

### II.5.2.3 Antimicrobial activity of oxytetracycline delivery systems

The antimicrobial activity of oxytetracycline-containing samples with 25% (wt) drug content was assessed against gram positive *Staphylococcus aureus* ATCC 25923, gram negative *E. coli* ATCC 25922 and *Pseudomonas aeruginosa* strains. After 24 h incubation, all prepared samples demonstrated good bactericidal activity similar to the drug powder (Fig.II.49). The best antimicrobial activity was observed against *Staphylococcus aureus* strain. The measured growth inhibition zone diameters for tested antibiotic-loaded samples were:  $34 \pm 2$  mm versus  $36 \pm 1$  mm of the positive control for *S. aureus*,  $30 \pm 2$  mm versus  $32 \pm 2$  mm for antibiotic in the case of *E. coli* and  $21 \pm 2$  mm versus  $22 \pm 1$  mm of control for *Pseudomonas aeruginosa* strain.

### II.5.4 Conclusions on the application of silica-titania mesoporous composites as carriers of biologically active molecules

The presence of titania nanoparticles on the silica surface can create stronger host-guest interactions between the support and oxytetracycline molecules because of donor-acceptor bonds formation in which titanium ions are involved. Doping the silica network with titanium ions modified the structural and pore wall surface properties of support, inducing a burst effect in the first stage of oxytetracycline delivery profiles, while the presence of the crystalline anatase on the silica surface contribute to a sustained drug release in the last stage, both altering the release mechanism. Thereby, controlling the distribution and content of titanium between the silica network and anatase phase is a promising strategy to develop oxytetracycline delivery systems with desired drug release profile, without affecting the bactericidal activity.

## II.6 Doxorubicin targeted delivery systems

The development of doxorubicin targeted delivery systems is very important considering its high toxicity. The magnetic composite materials used as carriers for doxorubicin, were obtained by coating the magnetite nanoparticles previously prepared by reducing Fe(III) tris(acetylacetonate) with  $\text{NaBH}_4$ , at room temperature followed by their coating with pristine and aminopropyl functionalized MCM-41 mesoporous silica (samples labelled  $\text{Fe}_3\text{O}_4@\text{MCM-41E}$  and  $\text{Fe}_3\text{O}_4@\text{MCM-APTES}$ , respectively). The coating of  $\text{Fe}_3\text{O}_4$  NPs with functionalized mesoporous silica was carried out by co-condensation. Subsequently,

$\text{Fe}_3\text{O}_4@\text{MCM-APTES}$  sample was modified with folate groups for targeting the tumor cell receptors, the synthesized material being labelled  $\text{Fe}_3\text{O}_4@\text{MCM-APTES-folate}$ . Another carrier tested was  $\text{Fe}_3\text{O}_4@\text{SBA-16}$ .

The doxorubicin targeted delivery systems with a drug content of 5% (wt.) or 10% (wt.) were obtained by incipient wetness impregnation method using a concentrated aqueous solution of cytostatic agent.

## II.6.2 Synthesis and characterization magnetic carriers

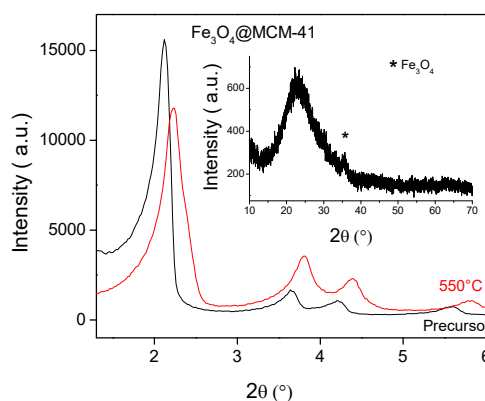


Fig.II.65 Small-angle XRD patterns of  $\text{Fe}_3\text{O}_4@\text{MCM-41E}$  (black curve),  $\text{Fe}_3\text{O}_4\text{-MCM-41}$  calcined at  $550^\circ\text{C}$  (red curve), respectively. Inset, the wide-angle XRD pattern of calcinated sample.

From the small-angle XRD patterns of magnetite nanoparticles coated with MCM-41 type silica can be noticed the formation of an ordered, hexagonal pore network, characteristic of this type of silica presenting the characteristic Bragg reflections (100), (110) and (200) (Fig.II.65). The wide-angle XRD patterns proved the preservation of magnetite crystalline structure and the formation of amorphous silica phase (Fig.II.65 inset).

The textural parameters of  $\text{Fe}_3\text{O}_4@\text{MCM-41E}$  composite material were determined by  $\text{N}_2$  adsorption-desorption isotherm recorded at 77 K. The adsorption-desorption isotherm is type IV, characteristic for mesoporous MCM-41-type materials, completely reversible with narrow pore size distribution. The textural parameters were calculated from the adsorption-desorption isotherm:  $S_{\text{BET}}=988 \text{ m}^2/\text{g}$ ,  $d_{\text{BJH}}=2.81 \text{ nm}$  and  $V_p=0.99 \text{ cm}^3/\text{g}$ , the synthesized composite material exhibiting a narrow pore size distribution and a high porosity.

The synthesized sample exhibited a superparamagnetic behavior due to nanometric particle size. The saturation magnetization value for the  $\text{Fe}_3\text{O}_4@\text{MCM-41E}$  sample was 1.4 emu/g, lower than the value for the used  $\text{Fe}_3\text{O}_4$  NPs for obtaining the magnetic composite material (50.04 emu /g).

*Encapsulation of magnetite nanoparticles in MCM-APTES and MCM-APTES-folate silica matrix as well as in the SBA-16 type silica*

The magnetization curve of  $\text{Fe}_3\text{O}_4@\text{MCM-APTES}$  material demonstrates also a superparamagnetic behaviour, the saturation magnetization value of 5.15 emu/g being higher than the one for  $\text{Fe}_3\text{O}_4@\text{MCM-41E}$  sample. Folate groups were linked on  $\text{Fe}_3\text{O}_4@\text{MCM-APTES}$  material by reaction between amine groups and folic acid in dimethylsulfoxide. The resulted material was further denoted  $\text{Fe}_3\text{O}_4@\text{MCM-APTES-folate}$ . This sample exhibited the highest saturation magnetization value (5.54 emu/g) from all the samples because of its high magnetite content.

The encapsulation of magnetite nanoparticles obtained by decomposing the  $\text{Fe}(\text{acac})_3$  in mesoporous SBA-16 silica matrix was performed according to the procedure reported in the literature using the Pluronic P123 triblock copolymer as structure directing agent. [10].

Table II.10 list the textural parameters determined from the  $\text{N}_2$  adsorption-desorption isotherms for the synthesized magnetic supports.

Table II.10 Textural parameters of magnetic composite materials

<i>Magnetic mesoporous matrix</i>	$S_{\text{BET}}$ (m <sup>2</sup> /g)	$V_{\text{pori}}$ (cm <sup>3</sup> /g)	$d_{\text{BJH}}$ des(nm)
Fe <sub>3</sub> O <sub>4</sub> @MCM-41E	988	0.99	2.81
Fe <sub>3</sub> O <sub>4</sub> @MCM-APTES	378	0.20	1.19
Fe <sub>3</sub> O <sub>4</sub> @SBA-16	938	0.70	9.10
Fe <sub>3</sub> O <sub>4</sub> @MCM-APTES-folate	118	0.80	3.70
Fe <sub>3</sub> O <sub>4</sub> @MCM-41(0.4)	612	0.51	2.66

Table II.11 Saturation magnetization and magnetic moment values for magnetic composite materials

Magnetic carriers	$M_s$ (emu/g)	$\mu/k$ (K/Oe)	Behavior
Fe <sub>3</sub> O <sub>4</sub> @MCM-41E	1.40	0.77	SPP
Fe <sub>3</sub> O <sub>4</sub> @MCM-APTES	5.15	1.16	SPP
Fe <sub>3</sub> O <sub>4</sub> @SBA-16	5.93	1.11	SPP
Fe <sub>3</sub> O <sub>4</sub> @MCM-APTES-folate	5.54	1.15	SPP

$M_s$  – saturation magnetization;  $\mu/k$  - magnetic moment divided by Boltzmann's constant; SPP - superparamagnetic behavior

### II.6.3 Synthesis and characterization doxorubicin targeted delivery systems

In this PhD thesis, it is used as vehicle for targeted delivery systems beside the carriers presented in this chapter, Fe<sub>3</sub>O<sub>4</sub>-MCM-41, a magnetic composite material whose synthesis and characterization is presented in chapters II.3.2 and II.4.1 to which the surfactant was removed by thermal treatment at 550 °C. The Fe<sub>3</sub>O<sub>4</sub>-MCM-41 (0.4) material has a magnetic particles content of 4.7 (wt.%).

Doxorubicin targeted delivery systems containing 5% and 10% cytostatic agent respectively were obtained by incipient wetness impregnation method using a concentrated aqueous solution of antibiotic.

FT-IR spectroscopy was used to assess the various functional groups bounded on mesoporous silica, and also doxorubicin molecules (Fig.II.74). The FTIR spectra of the mesoporous composite materials based on doxorubicin contained the characteristic vibrations of silica (1080 cm<sup>-1</sup>, 960 cm<sup>-1</sup>, 800 cm<sup>-1</sup>, 460 cm<sup>-1</sup>), the band characteristic of Fe(III)-O bonds at 640 cm<sup>-1</sup>, the bands of adsorbed water at 1650 cm<sup>-1</sup> and the bands of drug in the range of 2840-3000 cm<sup>-1</sup>, 1725 cm<sup>-1</sup>, 1290 cm<sup>-1</sup>. Also, in the FTIR spectra can be noticed characteristic vibrations for the methylene groups in the range of 2850-3000 cm<sup>-1</sup>, N-H symmetric and asymmetric stretching vibrations at 3300-3200 cm<sup>-1</sup> proving the successful mesoporous silica functionalization by co-condensation method with 3-aminopropyl groups (green curve). FTIR spectroscopy revealed the presence of the cytostatic agent in the mesoporous magnetic-silica transporters.

Wide-angle XRD analysis (Fig. II.76) of doxorubicin-loaded materials showed only the diffraction peaks characteristic to magnetite, along with the broad one in the range of 20-40° 2 $\theta$  attributed to the amorphous silica phase. In wide-angle XRD patterns, the diffraction peaks associated with doxorubicin cannot be observed, this being present in amorphous phase into the pores of mesoporous support. Table II.12 lists the textural parameters for doxorubicin-loaded materials obtained from N<sub>2</sub> absorption/desorption isotherms.

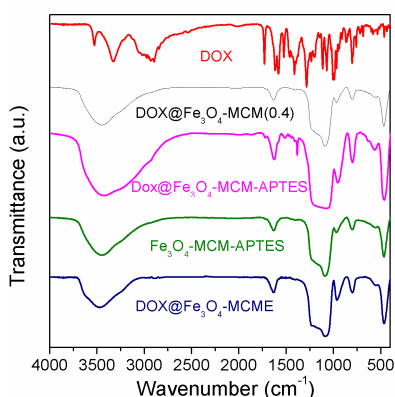


Fig.II.74 FTIR spectra of doxorubicin, carriers and doxorubicin-loaded samples

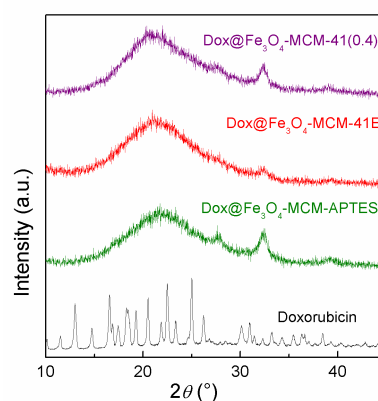


Fig.II.76 Wide-angle XRD patterns of doxorubicin and doxorubicin-loaded samples

Table II.12 Textural parameters of sample containing doxorubicin compared to the corresponding magnetic vehicles

Sample	Doxorubicin-loaded carrier			Magnetic mesoporous carrier			
	$S_{BET}$ (m <sup>2</sup> /g)	$V_{pori}$ (cm <sup>3</sup> /g)	$d_{BJH}$ (nm)	$S_{BET}$ (m <sup>2</sup> /g)	$V_{por}$ (cm <sup>3</sup> /g)	$d_{BJH}$ (nm)	$M_s$ (emu/g)
DOX@Fe <sub>3</sub> O <sub>4</sub> @MCM-41E	748	0.71	2.97	988	0.99	2.81	1.4
DOX@Fe <sub>3</sub> O <sub>4</sub> @MCM-41	477	0.47	2.66	612	0.51	2.66	3.77
DOX@Fe <sub>3</sub> O <sub>4</sub> @MCM-APTES	344	0.15	1.19	378	0.20	1.19	ND
DOX@Fe <sub>3</sub> O <sub>4</sub> @MCM-APTES-folate	N/A	N/A	N/A	118	0.80	3.70	5.54

#### II.6.4 *In vitro* doxorubicin release studies from magnetite-mesoporous silica-type carriers

Doxorubicin release profiles from magnetic vehicles were determined in saline phosphate buffer solution (PBS) pH 5.7, at 37 °C, simulating the tumoral cells environment. For the cytostatic agent, two concentrations in PBS were used, 0.033 and 0.016 g DOX /L PBS. At high tested DOX concentration, its dissolution reaches about 65% (wt) (Fig. II.79 A.DOX curve), while for low concentration of 0.016 g/L, the entire amount of drug (B.DOX curve) was dissolved. Thus, the method B using 0.016 g of DOX / L medium is the optimum procedure for determination of *in vitro* drug release profiles.

The aminopropyl functionalization of silica layer led to an increase of the doxorubicin release rate in the first stage, but also to a decrease in the sustained release step (after ~ 8 hours).

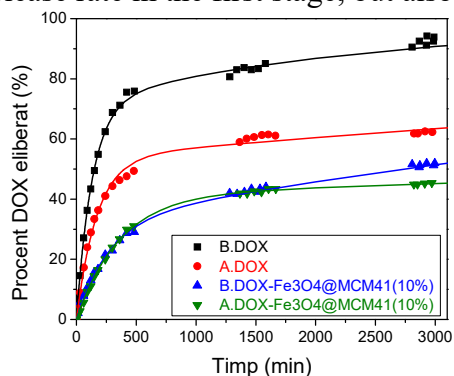


Fig.II.79 Doxorubicin release profiles from Fe<sub>3</sub>O<sub>4</sub>@MCM-41E vehicle at different drug concentration in PBS in comparison with the drug dissolution curves.

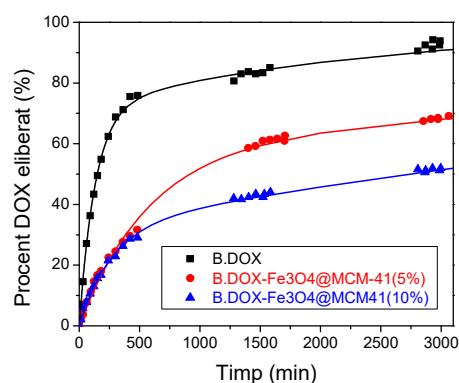


Fig. II.80 Comparison of doxorubicin release profiles for Fe<sub>3</sub>O<sub>4</sub>@MCM-41 with a different drug content of 5% and 10%

Table II.13 Doxorubicin Release Experiments

Sample	DOX/ PBS ( $g L^{-1}$ )
A.DOX	0.033
A.DOX-Fe <sub>3</sub> O <sub>4</sub> @MCM-41 (10%)	0.033
B.DOX	0.016
B.DOX- Fe <sub>3</sub> O <sub>4</sub> @MCM-41(10%)	0.016
B.DOX- Fe <sub>3</sub> O <sub>4</sub> @MCM-41(5%)	0.016
B.DOX- Fe <sub>3</sub> O <sub>4</sub> @SBA-16 (5%)	0.016
B.DOX- Fe <sub>3</sub> O <sub>4</sub> @MCM-APTES	0.016

This observation could be explained by the existence of repulsive electrostatic interactions between positively charged amino groups linked to the carrier pore surface and partially protonated doxorubicin. Unlike the MCM-41 material, SBA-16 silica has a cubic framework of interconnected pores [10], which favors the drug diffusion. A faster release kinetics for DOX-Fe<sub>3</sub>O<sub>4</sub>@SBA-16 sample similar to doxorubicin dissolution curve can be observed.

All experimental drug release data were fitted using the three-parameter theoretical kinetic model. This model assumes the existence of the both organic molecules, which are strongly adsorbed on the mesopores surface (associated molecules) and the free molecules into the mesochannels (dissociated molecules). Between these two types of molecules there is an equilibrium, characterized by  $k_{on}$  and  $k_{off}$  rate constants, corresponding to the association and dissociation processes. It is assumed that both processes follow a first order kinetics. Dissociated molecules can be released into the simulated body fluid through a diffusion process, with the rate constant  $k_s$ , which is a first order kinetics process.

Doxorubicin release kinetics from Fe<sub>3</sub>O<sub>4</sub>@MCM-APTES-folate material (Fig.II.82) is slow both in the *burst* step and sustained release stage, 44.7% and about 60% from encapsulated drug being released in the first 24 hours and after 48 hours, respectively.

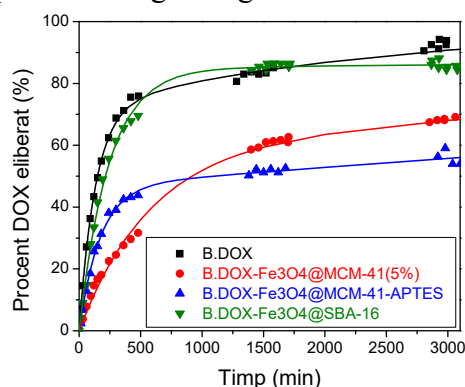


Fig.II.81 Comparison of doxorubicin release profiles for Fe<sub>3</sub>O<sub>4</sub>@MCM-41, Fe<sub>3</sub>O<sub>4</sub>@MCM-APTES and Fe<sub>3</sub>O<sub>4</sub>@SBA-16 carriers

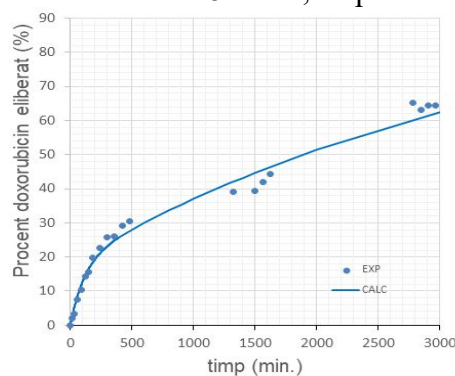


Fig. II.82 Doxorubicin release profile for the Fe<sub>3</sub>O<sub>4</sub>@MCM-APTES-folate carrier

The release rate is directly proportional with the diffusion constant,  $k_s$ , due to the dissociated drug molecules, which are released in the first stage because the weak interactions between doxorubicin and the carrier. After the dissociated molecules release, the limiting process becomes the dissociation of associated molecules, and the sustained release rate (second stage of the release process) is directly proportional to the dissociation constant,  $k_{off}$ . Negative values of  $\Delta G$  indicates a small amount of drug released in the first release stage, desirable to minimize the cytostatic agent side effects. The best carriers are Fe<sub>3</sub>O<sub>4</sub>@MCM-APTES and Fe<sub>3</sub>O<sub>4</sub>@MCM-APTES-folate.

Table II.14 Parameters of kinetic model for the developed doxorubicin-based targeted drug delivery systems

Sample	$\Delta G$ ( $10^{-21}$ J)	$k_s$ ( $10^{-3}\text{min}^{-1}$ )	$k_{\text{off}}$ ( $10^{-5}\text{min}^{-1}$ )	$k_{\text{on}}$ ( $10^{-5}\text{min}^{-1}$ )	$R^2$
A.DOX	0.85	5.8	8.1	6.7	0.9966
A.DOX-Fe <sub>3</sub> O <sub>4</sub> @MCM-41(10%)	-1.34	2.7	2.4	3.2	0.9997
B.DOX	4.65	7.4	42.5	14.3	0.9987
B.DOX-Fe <sub>3</sub> O <sub>4</sub> @MCM-41(10%)	-2.36	3.5	12.2	21.2	0.9990
B.DOX-Fe <sub>3</sub> O <sub>4</sub> @MCM-41(5%)	2.22	1.7	10.5	6.2	0.9982
B.DOX-Fe <sub>3</sub> O <sub>4</sub> @SBA-16	7.42	4.1	2.9	0.5	0.9984
B.DOX-Fe <sub>3</sub> O <sub>4</sub> @MCM-APTES	-4.03	5.8	6.5	7.1	0.9963
B.DOX-Fe <sub>3</sub> O <sub>4</sub> @MCM-APTES-folate	-5.06	7.83	30.7	10.0	0.9875

## II.6.5 Toxicity assays on doxorubicin targeted delivery systems

A selection of the doxorubicin-targeted delivery systems developed in this PhD thesis was tested on a human lymphocytic cell line. The cell viability was analyzed using CellTiter 96<sup>®</sup>AQ<sub>ueous</sub> one solution (MTS kit) from Promega. DOX-Fe<sub>3</sub>O<sub>4</sub>@MCM-41 and DOX-Fe<sub>3</sub>O<sub>4</sub>MCM-APTES-folate samples with 5% (wt) doxorubicin were chosen for the cytotoxicity evaluation.

One can notice lower toxicity of doxorubicin encapsulated in a magnetic mesoporous carrier than the case when cells were treated with doxorubicin aqueous solution in the same concentration as in the release experiments. The cytotoxicity of either the samples containing encapsulated cytostatic agent, or doxorubicin is slightly higher after 48 hours than after 24 hours (Fig.II.83).

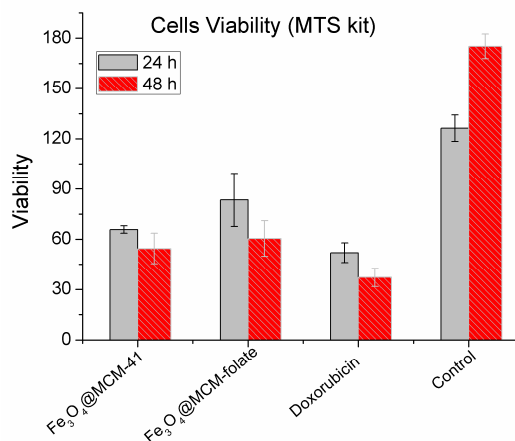


Fig. II.83 Cell viability of selected doxorubicin targeted delivery systems in comparison with doxorubicin

## II.7 Final remarks

In this PhD thesis were synthesized and characterized ferrite-silica MCM-41-type and silica-titania SBA-15-type composites. The model drug molecules, which were used for the development of drug delivery systems were oxytetracycline and doxorubicin. For the obtained drug delivery systems were studied *in vitro* release profiles by UV-vis spectroscopy. Both synthesized carriers and drug delivery systems obtained during the PhD studies were characterized by various techniques: FTIR spectroscopy, small- and wide-angle XRD, nitrogen adsorption-desorption isotherms, scanning and transmission electron microscopy, magnetic

measurements at room temperature etc. in order to determine their structure and properties and to understand the interactions between biologically active molecules and synthesized vehicles.

To fulfill the aim of this PhD thesis, the development of drug-targeted delivery systems, several activities have been carried out which have contributed to the achievement of the assumed objectives:

(i) Synthesis of magnetite and cobalt ferrite nanoparticles with inverse spinel structure and cubic symmetry by co-precipitation or decomposition of iron(III) tris(acetylacetonate), using different compounds as stabilizer, oleic acid, triblock copolymer Pluronic P123, or cetyltrimethyl ammonium bromide. *For the first time it was obtained crystalline cobalt ferrite at low temperature, 60°C directly in the reaction medium.* All synthesized magnetite samples showed superparamagnetic behavior, with a single magnetic domain, while cobalt ferrite nanoparticles exhibited ferromagnetic properties.

The highest specific surface area values of ferrite nanoparticles were obtained in the presence of Pluronic P123, magnetite and cobalt ferrite being mesoporous materials. The saturation magnetization value (52.33 emu/g) was higher for ferrite obtained in the presence of oleic acid. The highest value of saturation magnetization (59.81 emu/g) was obtained for magnetite synthesized in the presence of CTAB.

(ii) Mesoporous ferrite-silica composites were synthesized using two approaches: one-step method applied for the preparation of Fe<sub>3</sub>O<sub>4</sub>-MCM-41 composite material without the isolation of the magnetite nanoparticles (further applied as vehicle for doxorubicin) and the two steps procedure, in which magnetite or the cobalt ferrite nanoparticles were first synthesized and isolated, then re-dispersed in water and coated with mesoporous MCM-41 silica. The coating procedure was performed by sol-gel method, assisted by hydrothermal treatment at 100 °C, 24 h. In the first case, magnetite was prepared in the presence of CTAB, and in the second case, magnetite or cobalt ferrite nanoparticles were prepared using oleic acid as stabilizer. The magnetisation curves of magnetic composite materials containing magnetite did not have hysteresis exhibiting superparamagnetic properties, while CoFe<sub>2</sub>O<sub>4</sub>-MCM sample presented ferrimagnetic properties. The remnant magnetization and coercivity of CoFe<sub>2</sub>O<sub>4</sub>-MCM material were 0.38 emu/g and 427 Oe, respectively. For synthesized CoFe<sub>2</sub>O<sub>4</sub>-MCM composite with 3.10% (wt.) magnetic phase the saturation magnetization value was 1.26 emu/g.

The cytotoxicity of ferrite-mesoporous silica composite materials at different concentrations (50, 100 and 200 µg / mL) was evaluated on oposum kidney cell line and the cell viability was not altered significantly, demonstrating no toxicity at tested nanoparticles concentration.

Fe<sub>3</sub>O<sub>4</sub>@MCM-41E composite material was obtained by coating the magnetite nanoparticles previously obtained in the presence of CTAB with MCM-41 silica. Magnetite nanoparticles are well dispersed into MCM-41 silica matrix. Fe<sub>3</sub>O<sub>4</sub>@MCM-41E composite exhibited the highest saturation magnetisation value from the obtained Fe<sub>3</sub>O<sub>4</sub>@MCM-41-type composite materials, but its specific surface area and pore volume values were lower than for the other samples.

(iii) Mesostructured silica-titania SBA-15-type composites containing 4,5, 10, 20 and 30% (mol) titanium were obtained in the presence of Pluronic P123 as structure directing agent, by sol-gel technique combined with a hydrothermal treatment, characterized and further explored as carriers for a model molecule, oxytetracycline.

All synthesized silica-titania composites showed an ordered mesophase and the presence of anatase phase, except for Ti4.5SBA-15 material for which the anatase phase is hardly detectable because of its low titanium content, suggesting that titanium is mostly incorporated into the silica matrix by replacing silicon atoms. Silica-titania composites were compared with SBA-15 silica and mesoporous titania.

(iv) Oxytetracycline delivery systems based on inorganic silica-titania carriers with a drug content of 25% (wt.) or 33% (wt.) were obtained by incipient wetness impregnation method using a concentrated aqueous solution of antibiotic. The oxytetracycline release profiles were

determined in PBS solution pH 5.7, at 37 ° C. The crystalline titania phase, located on the silica surface, led to a slower release kinetics of antibiotic molecules. The lowest sustained release rate was noticed for silica-titania composite with 10% (mol) titanium content mainly due to particles morphology. For Ti4.5SBA-15 carrier for both drug concentrations, the drug release profiles are similar to those from SBA-15 silica, with the most pronounced *burst* effect. For samples having a lower drug content, a slower release rate of antibiotic molecules was observed in the first step of delivery profile. The presence of anatase nanoparticles on the silica surface led to a reduction of the release rate, which was more pronounced with the increase of titanium content. All tested oxytetracycline delivery systems showed good bactericidal activity similar to antibiotic, demonstrating that the antimicrobial activity was not affected by drug adsorption into inorganic carrier mesopores. Designing of mesoporous silica-titania carriers with optimal titanium content is required to obtain effective drug delivery systems.

(iv) *Elaboration of doxorubicin targeted delivery systems by using magnetite-mesoporous MCM-41-type silica vehicles with adequate absorbent capacity and superparamagnetic properties.* All synthesized and characterized magnetite coated with MCM-41-type silica carriers exhibited superparamagnetic behavior and enough porosity to accommodate the required amount of cytostatic agent. The highest values of saturation magnetization were obtained for functionalized carriers, Fe<sub>3</sub>O<sub>4</sub>@MCM-APTES-folate (5.54 emu/g) and Fe<sub>3</sub>O<sub>4</sub>@MCM-APTES (5.15 emu/g). A high saturation magnetization value for the carrier is necessary to deliver drug molecules into the targeted tissue.

The doxorubicin release profiles were determined in saline phosphate buffer solution pH 5.7 at 37°C, simulating tumor cell environment. Two encapsulated drug content in 5% and 10% (wt) into magnetic carriers were studied. The effective encapsulation of cytostatic agent in the proposed magnetic vehicles was demonstrated, especially in the case of Fe<sub>3</sub>O<sub>4</sub>@MCM-APTES material, the drug release profiles being very slow, which would target tumor tissue by applying a magnetic field or passive accumulation through folate groups linked on silica surface.

The cytotoxicity of selected doxorubicin targeted delivery systems was tested on a healthy human lymphocyte cell line. The tests demonstrated a lower toxicity of doxorubicin when it is encapsulated in mesoporous silica-magnetite carriers than when it is applying as an aqueous solution in the same concentration.

### ***Original contributions***

- Synthesis and characterization of drug delivery systems containing SBA-15-type mesostructured silica-titania composites. Comparison of the properties of mesostructured silica-titania composites with those of SBA-15 silica and mesoporous titania. In this case, the model drug was oxytetracycline.
- Obtaining for the first time crystalline cobalt ferrite by coprecipitation method, directly from aqueous solution, at low temperature, 60 °C.
- Cytotoxicity evaluation of synthesized cobalt ferrite/magnetite coated with MCM-41-type mesoporous silica depending on their concentration.
- Encapsulation of doxorubicin into magnetic vehicles, magnetite-mesoporous silica functionalized with APTES or folate groups for passive accumulation in tumor tissue with reduced toxic effects compared with the cytostatic agent administered as an aqueous solution.

### ***Perspectives***

- Development of mesoporous silica coated cobalt ferrite materials, which demonstrated low cytotoxicity, for other applications.
- Testing of mesostructured silica-titania composites as carriers for other drug molecules or photocatalysis.
- Cytotoxicity studies on different healthy and tumor cell lines of doxorubicin targeted delivery systems.
- Development of other drug delivery systems based on mesoporous titania.

#### PUBLISHED ARTICLES

- 1/ R.-A. Mitran, **D. Georgescu**, N. Stănică, C. Matei, D. Berger, Acoperirea nanoparticulelor de magnetită cu un strat de silice mezoporoasă cu pori de dimensiuni și geometrii diferite/Coating magnetite nanoparticles with mesostructured silica shell of different pore and geometry, *Revista Română de Materiale/Romanian Journal of Materials*, 46 (2016), 296-302.
- 2/ D. Berger, **D. Georgescu**, L. Băjenaru, A. Zanfir, N. Stănică, C. Matei, Properties of mesostructured silica coated  $\text{CoFe}_2\text{O}_4$  versus  $\text{Fe}_3\text{O}_4$ -silica composites, *Journal of Alloys and Compounds*, 708 (2017) 278-284.
- 3/ **D. Georgescu**, C. Matei, N. Stănică, D. Berger, Mesoporous ferrite obtained in the presence of pluronic copolymer for potential biomedical applications, *UPB Scientific Bulletin*, Series B, 79 (2017) 13-22.
- 4/ **D. Georgescu**, A.-M. Brezoiu, R.-A. Mitran, D. Berger, C. Matei, B. Negreanu-Pirjol Mesostructured silica-titania composites for improved oxytetracycline delivery systems, *Comptes Rendus Chimie*, 20 (2017) 1017-1025.

#### SCIENTIFIC MANIFESTATIONS

- 1/ Faculty of Chemistry Conference, „Alexandru Ioan Cuza” University Days, Iași, 29-31 October 2015  
Poster presentation „Magnetic mesoporous inorganic composites with biomedical applications”, authors D. Georgescu, A. Zanfir, N. Stănică, R.A. Mitran, C. Munteanu, C. Matei, D. Berger.  
Obtained results: DIPLOMĂ PENTRU REZULTATE DEOSEBITE ÎN ACTIVITATEA DE CERCETARE ȘTIINȚIFICĂ, Iași 29-31 Octombrie 2015.
- 2/ National Institute for Research & Development in Chemistry & Petrochemistry ICECHIM, International symposium Priorities of Chemistry for a Sustainable Development PRIOCHEM 12 th Edition Bucharest 27-29 octombrie 2016.  
Poster presentation „OXYTETRACYCLINE DELIVERY SYSTEMS CONTAINING MESOPOROUS SILICA-TITANIA COMPOSITES”, authors **D. Georgescu**, A.M. Brezoiu, R.A. Mitran, B. Negreanu-Pirjol, C. Matei, D. Berger.

## References (selection)

- [1] J.C.Cezar, M.Knobel, H.C.N.Tolentino, Magnetic properties of Cu-Permalloy granular alloy, *Journal of Magnetism and Magnetic Materials*, 226-230 (2001) 1519-1521.
- [2] M.Kuźmiński, A.Ślawska-Waniewska, H.K.Lachowicz, M.Knobel, The effect of particle size and surface-to-volume ratio distribution on giant magnetoresistance (GMR) in melt-spun Cu-Co alloys, *Journal of Magnetism and Magnetic Materials*, 205 (1999) 7-13.
- [6] **D.Georgescu, C.Matei, N.Stănică, D.Berger, Mesoporous ferrite obtained in the presence of pluronic copolymer for potential biomedical applications, *UPB Scientific Bulletin, Series B*, 79 (2017) 13-22.**
- [7] P.E.G.Casillas, C.A.M.Pérez, C.A.R.Gonzalez (2012), Infrared Spectroscopy – Materials Science, Engineering and Technology, *INTECH Open Access Publisher*, (2012) 405-420.
- [8] A.B.Salunkhe, V.M.Khot, N.D.Thorat, M.R.Phadatare, C.I.Sathish, D.S.Dhawale, S.H. Pawar, Polyvinyl alcohol functionalized cobalt ferrite nanoparticles for biomedical applications, *Journal Applied surface science*, 264 (2013) 598– 604.
- [9] C.I.Covaliu, C.Matei, A.C.Ianculescu, I.Jitaru, D.Berger, Fe<sub>3</sub>O<sub>4</sub>, CoFe<sub>2</sub>O<sub>4</sub> nanoparticles stabilized in sodium alginate polymer, *UPB Scientific Bulletin, Series B: Chemistry and Materials Science*, 71 (2009) 53-60.
- [10] **R.A.Mitran, D.Georgescu, N.Stănică, C.Matei, D.Berger, Coating magnetite nanoparticles with mesostructured silica shell of different pore size and geometry, *Revista Română de Materiale / Romanian Journal of Materials*, 46 (2016) 437 – 443.**
- [11] **D.Berger, D.Georgescu, L.Băjenaru, A.Zanfir, N.Stănică, C.Matei, Properties of mesostructured silica coated CoFe<sub>2</sub>O<sub>4</sub> versus Fe<sub>3</sub>O<sub>4</sub>-silica composites, *Journal of Alloys and Compounds*, 708 (2017), 278-284.**
- [14] J.Kim, J.E.Lee, J.Lee, J.Ho Yu, B.C.Kim, K.An, Y.Hwang, C.-H.Shin, J.-G.Park, J.Kim, T.Hyeon, Magnetic fluorescent delivery vehicle using uniform mesoporous silica spheres embedded with monodisperse magnetic and semiconductor nanocrystals, *Journal of the American Chemical Society*, 128 (2006) 688-689.
- [15] R.A.Bohara, N.D.Thorat, H.M.Yadav, S.H.Pawar, One-step synthesis of uniform and biocompatible amine functionalized cobalt ferrite nanoparticles: a potential carrier for biomedical applications, *New Journal of Chemistry*, 38 (2014) 2979-2986.
- [16] P.Pradhan, J.Giri, G.Samanta, H.D.Sarma, K.P.Mishra, J.Bellare, R.Banerjee, D.Bahadur, Comparative evaluation of heating ability and biocompatibility of different ferrite-based magnetic fluids for hyperthermia application, *Journal of Biomedical Materials Research Part B: Applied Biomaterials*, 81B (2007) 12-22.
- [17] G.Aygar, M.Kaya, N.Özkan, S.Kocabıyık, M.Volkan, Preparation of silica coated cobalt ferrite magnetic nanoparticles for the purification of histidine-tagged proteins, *Journal of Physics and Chemistry of Solids*, 87 (2015) 64-71.
- [18] L.E.Euliss, S.G.Grancharov, S.O'Brien, T.J.Deming, G.D.Stucky, C.B.Murray, G.A.Held, Cooperative assembly of magnetic nanoparticles and block copolypeptides in aqueous media, *Nano Letters*, 3 (2003) 1489-1493.
- [19] X.Liu, Y.Guan, Z.Ma, H.Liu, Surface modification and characterization of magnetic polymer nanospheres prepared by miniemulsion polymerization, *Langmuir*, 20 (2004) 10278-10282.
- [20] R.Hong, N.O.Fischer, T.Emrick, V.M.Rotello, Surface PEGylation and Ligand Exchange Chemistry of FePt Nanoparticles for Biological Applications, *Chemistry of Materials*, 17 (2005) 4617-4621.
- [21] Y.Sahoo, H.Pizem, T.Fried, D.Golodnitsky, L.Burstein, C.N.Sukenik, G.Markovich, Alkyl Phosphonate/Phosphate Coating on Magnetite Nanoparticles: A Comparison with Fatty Acids, *Langmuir*, 17 (2001) 7907-7911.
- [22] M.Kim, Y.Chen, Y.Liu, X.Peng, Super-Stable, High-Quality Fe<sub>3</sub>O<sub>4</sub> Dendron–Nanocrystals Dispersible in Both Organic and Aqueous Solutions, *Advanced Materials*, 17 (2005) 1429-1432.
- [23] Y.Kobayashi, M.Horie, M.Konno, B.Rodríguez- González, L.M.Liz- Marzán, Preparation and Properties of Silica-Coated Cobalt Nanoparticles, *J. Phys. Chem. B*, 107 (2003) 7420-7425.
- [24] A.-H.Lu, W.-C.Li, N.Matoussevitch, B.Splithoff, H.Bönnemann, F.Schüth, Highly stable carbon-protected cobalt nanoparticles and graphite shells, *Chemical Communication*, 0 (2005) 98-100.
- [25] N.S.Sobal, M.Hilgendorff, H.Möhwald, M.Giersig, M.Spasova, T.Radetic, M.Farle, Synthesis and Structure of Colloidal Bimetallic Nanocrystals: The Non-Alloying System Ag/Co *Nano Letters*, 2 (2001) 621–624.

- [26] Q.Liu, Z.Xu, J.A.Finch, R.Egerton, A Novel Two-Step Silica-Coating Process for Engineering Magnetic Nanocomposites, *Chemistry of Materials*, 10 (1998) 3936-3940.
- [27] J.Lin, W.Zhou, A.Kumbhar, J.Wiemann, J.Fang, E.E.Carpenter, C.J.O'Connor, Gold-Coated Iron (Fe@Au) Nanoparticles: Synthesis, Characterization, and Magnetic Field-Induced Self-Assembly, *Journal of Solid State Chemistry*, 2001, 159 (2001) 26-31.
- [28] N.O.Núñez, P.Tartaj, M.P.Morales, P.Bonville, C. J. Serna, Yttria-Coated FeCo Magnetic Nanoneedles, *Chemistry of Materials*, 16 (2004) 3119-3124.
- [36] H.H.P.Yiu, M.A.Keane, Z.A.Lethbridge, M.R.Lees, A.J.El Haj, J.Dobson, Synthesis of novel magnetic iron metal-silica (Fe-SBA-15) and magnetite-silica (Fe<sub>3</sub>O<sub>4</sub>-SBA-15) nanocomposites with a high iron content using temperature-programed reduction, *Nanotechnology*, 19 (2008) 255606.
- [37] X.Zang, W.Xie, Enzymatic interesterification of soybean oil and methyl stearate blends using lipase immobilized on magnetic Fe<sub>3</sub>O<sub>4</sub>/SBA-15 composites as a biocatalyst, *Journal of Oleo Science*, 63 (2014), 1027-1034.
- [39] H.R.Emamian, A.Honarbakshsh-Raouf, A.Ataie, A.Yourdkhani, Synthesis and magnetic characterization of MCM-41/CoFe<sub>2</sub>O<sub>4</sub> nano-composite, *Journal of Alloys and Compounds*, 480 (2009) 681-683.
- [40] I.S.Lyubutin, S.S.Starchikov, N.E.Gervits, N.Yu.Korotkov, T.V.Dmitrieva, C.R.Lin, Y.T.Tseng, K.Y.Shih, J.S.Lee, C.C.Wang, Canted spin structure and the first order magnetic transition in CoFe<sub>2</sub>O<sub>4</sub> nanoparticles coated by amorphous silica, *Journal of Magnetism and Magnetic Materials*, 415 (2016) 13-19.
- [41] M.V.Berridge, A.S.Tan, Characterization of the cellular reduction of 3-(4,5-dimethylthiazol-2-yl)-2,5-diphenyltetrazolium bromide (MTT): subcellular localization, substrate dependence, and involvement of mitochondrial electron transport in MTT reduction. *Archives of Biochemistry and Biophysics*, 303 (1993) 474-482.
- [42] T.Bernas, J.W.Dobrucki, The role of plasma membrane in bioreduction of two tetrazolium salts, MTT and CTC, *Archives of Biochemistry and Biophysics*, 380 (2000) 108-116.
- [43] V.Pašukonienė, A.Mlynska, S.Steponkienė, V.Poderys, M.Matulionytė, V.Karabanovas, U.Statkutė, R.Purvinienė, J.A.Kraško, A.Jagminas, M.Kurtinaitienė, M.Strioga, R.Rotomskis, Accumulation and biological effects of cobalt ferrite nanoparticles in human pancreatic and ovarian cancer cells, *Medicina* 50 (2014) 237-244.
- [44] S.Sabale, V.Jadhav, V.Khot, X.Zhu, M.Xin, H.Chen, Superparamagnetic MFe<sub>2</sub>O<sub>4</sub> (M=Ni, Co, Zn, Mn) nanoparticles: synthesis, characterization, induction heating and cell viability studies for cancer hyperthermia applications, *Journal of Materials Science: Materials in Medicine*, 26 (2015) 127.
- [45] K.S.W.Sing, Reporting physisorption data for gas/solid systems with special reference to the determination of surface area and porosity (Recommendations 1984), *Pure and Applied Chemistry*, 57 (1985) 603-619.
- [46] J.C.Groen, L.A.A.Peffer, J.Pérez-Ramírez, Pore size determination in modified micro- and mesoporous materials. Pitfalls and limitations in gas adsorption data analysis, *Microporous and Mesoporous Materials*, 60 (2003), 1-17.
- [47] S.Y.Chen, T.Mochizuki, Y.Abe, M.Toba, Y.Yoshimura, Ti-incorporated SBA-15 mesoporous silica as an efficient and robust Lewis solid acid catalyst for the production of high-quality biodiesel fuels, *Applied Catalysis B: Environmental*, 148-149 (2014) 344-356.
- [48] D.Georgescu, A.-M.Brezoiu, R.-A.Mitran, D.Berger, C.Matei, B.Negreanu-Pirjol Mesostructured silica-titania composites for improved oxytetracycline delivery systems, *Comptes Rendus Chimie*, 20 (2017) 1017-1025 .**
- [49] M.M.Wan, X.D.Sun, S.Liu, J.Ma, J.H.Zhu, Versatile drug releaser derived from the Ti-substituted mesoporous silica SBA-15, *Microporous and Mesoporous Materials*, 199 (2014) 40-49.
- [50] L.Yang, Z.Jiang, S.Lai, C.Jiang, H.Zhon, Synthesis of Titanium Containing SBA-15 and Its Application for Photocatalytic Degradation of Phenol, *International Journal of Chemical Engineering*, 2014 (2014) 691562 7 pagini.